

Micro-Imaging Employed to Study Diffusion and Surface Permeation in Porous Materials

Von der Fakultät für Physik und Geowissenschaften

der Universität Leipzig

genemigte

DISSERTATION

zur Erlangung des akademischen Grades

doctor rerum naturalium

Dr. rer. nat.

vorgelegt

von Diplomphysiker Florian Hibbe,

geboren am 01. Januar 1983 in Soltau

Gutachter: Prof. Dr. Jörg Kärger

Prof. Dr. Bernd Smarsly

Tag der Verleihung 20. Dezember 2012

Abstract

Hibbe, Florian

*Micro-Imaging Employed to Study Diffusion and Surface Permeation
in Porous Materials*

Universität Leipzig, Dissertation

78 pages, 103 references, 34 figures, 6 tables, 2 attachments

This thesis summarizes experimental results on mass transport of small hydrocarbons in micro-porous crystals obtained via interference microscopy (IFM). The transport process has been investigated in three different materials with different pore structures : the metal-organic framework Zn(tbip) with one-dimensional pores, a FER type zeolite with two-dimensional anisotropic pore structure and zeolite A, a LTA type material with isotropic three-dimensional pore structure.

Mass transport is described in terms of diffusivity and surface permeability, both derived from the detected transient concentration profiles. The results on intra-crystalline diffusion are discussed under consideration of the influences of pore diameter and molecule diameter, which are both found to have a strong influence on the diffusivity.

Based on experimental results measured on the Zn(tbip) material, a new model for the description of surface barriers is developed and proved by experiment. It is demonstrated that the observed surface barrier is created by the total blockage of a large number of pore entrances at the surface and not by a homogeneous surface layer.

Contents

1	Introduction	1
1.1	Overview	1
1.2	Motivation	1
1.3	Diffusion Micro Imaging	3
2	Methods and Materials	6
2.1	Interference Microscopy	6
2.2	Porous Materials	9
2.2.1	General	9
2.2.2	Zeolites	10
2.2.3	Metal-Organic Framework – MOFs	10
2.3	Diffusion and Mass Transport	11
2.3.1	Diffusion Basics	11
2.3.2	Diffusion in Porous Materials	13
2.3.3	Temperature Effects	15
2.4	Data Analysis	15
2.4.1	Integral Uptake Curves	15
2.4.2	1d Concentration Profiles	16
2.4.3	2d and 3d Profiles	17
2.4.4	Accuracy of Diffusivity and Permeability Data	17
2.5	Observation Window	18
3	MOF Zn(tbip)	20
3.1	Material Description	20
3.2	Diffusion and Surface Permeation in Zn(tbip)	20
3.3	A Model for Surface Permeation and Diffusion in Zn(tbip)	22
3.4	Aging Effects on MOF Zn(tbip) due to Storage	28
4	Diffusion in FER Type Zeolite	33
4.1	Motivation	33
4.2	Diffusion of Methanol in Ferrierite	35

4.2.1	Diffusion in 8-Ring Channels at Elevated Temperatures	35
4.2.2	Diffusion Anisotropy	42
4.3	AFM Investigation of FER Surfaces	48
4.4	Other Molecules in Ferrierite	52
4.4.1	Overview	52
4.4.2	Pre-Sorption of Ethanol	54
5	AIPO-LTA	59
5.1	LTA in AIPO Form	59
5.1.1	LTA and other 8 Member Ring Materials	59
5.1.2	Template Removal in ALPO-LTA	60
5.2	Investigations of Mass Transport in AIPO-LTA	61
5.2.1	IFM Experiments	61
5.2.2	In Larger Context	66
6	Summary	70
7	Attachment	A
7.1	Curriculum Vitae	B
7.2	Danksagung	C

Symbols Used

Symbol	Unit	Meaning
α	[m s ⁻¹]	surface permeability
$c_{app}(x, y)$	a.u.	apparent concentration measured by interference or IR microscopy
$c(x, y, z)$	a.u.	local concentration of guest molecules
D	[m ² s ⁻¹]	transport diffusivity
D_s	[m ² s ⁻¹]	self-diffusivity
D_0	[m ² s ⁻¹]	corrected diffusivity
E_A	[kJ mol ⁻¹]	activation energy
E_λ	–	extinction at wavelength λ
ϵ_λ	[m ² mol ⁻¹]	extinction coefficient at wavelength λ
\vec{j}	[molecules s ⁻¹ m ²]	flux of guest molecules
λ	[m]	wave length
$l_{x,y}$	[m]	half crystal length in x - or y -direction
$L(x, y)$	[m]	thickness of the studied material in observation (z -) direction
$m(t)$	a.u.	loading
n	–	refractive index
φ	–	phase angle
$\Delta\varphi$	–	phase difference
p	mbar	pressure
R	[J mol ⁻¹ K ⁻¹]	gas constant
T	[K]	temperature
t	[s]	time
Γ	–	thermodynamic factor

Chapter 1

Introduction

1.1 Overview

The scope of this work is the experimental investigation, analysis and interpretation of mass transport in porous materials. It is structured in the following way:

The '*Introduction*' should give a motivation for the investigation of mass transport in porous media as well as an overview over the applied experimental techniques and the scientific state of art.

In the '*Materials and Methods*' chapter the experimental technique employed to obtain most of the experimental results (interference microscopy, IFM) and the examined porous materials are introduced.

The next three chapters present the experimental results. Each chapter is dedicated to one of the investigated porous materials which differ in their chemical composition, their shape and, most importantly, for their mass transport properties, their pore structure.

The thesis is concluded by a summary of the main findings of the experimental work followed by the attachment section in which additional experimental data and further supporting material is collected.

1.2 Motivation

Porous materials are widely used as catalysts, adsorbents and molecular sieves in technical and industrial processes [1, 2]. In the large family of porous materials zeolites are one of the most important and industrially best established representatives with an annual consumption of more than 6 million tons, corresponding to an estimated market value of about 2 billion euro in 2005 [3]. During the last years big efforts have been made to develop other and superior materials such as metal organic framework (MOF) crystals and

porous glasses in order to replace zeolites, but while the new materials often show improved features, for example in terms of better storage capability in the case of MOFs or better formability in the case of porous glasses, zeolites have not been replaced in the majority of applications.

The investigation of mass transport in porous crystals is motivated from questions of both, fundamental research and practical applications. In many applications mass transport on the molecular level is of crucial importance, demanding a detailed fundamental understanding of the transport mechanism in and into porous materials [4, 5], as even small improvements in performance can result in a big profit increase. Due to their well-defined morphology, porous crystallites are supposed to be ideal model systems to prove and test concepts of diffusion theory in porous media and to improve the understanding of host-guest interactions in such sophisticated materials [6].

Although many aspects of molecular transport in microporous materials are well understood after many years of intensive research, a lot of questions are still open and discussed intensively. The synthesis of porous materials is still a challenging and complicated task, especially with respect to the reproducibility of recently discovered materials. This and the different strengths and weaknesses of the variety of experimental techniques employed to study transport phenomena based on diffusion (see Tab 1.1) often lead to diverging results published in literature [7–11] and strongly demand further investigations in this field.

The transport properties of these materials – which are, again, of main interest in most technical applications – can be studied exclusively in non-equilibrium experiments. The techniques applied to study mass transport can roughly be categorized by their spatial resolution in *macroscopic* and *microscopic* techniques [2, 5]. As a rule of thumb *macroscopic* techniques are often batch-techniques that derive their results from the mean response of the system to a swing in the surrounding concentration of probe molecules (*Zero Length Column* (ZLC) technique [12], *Frequency Response* technique [13], sorption rate techniques [14]). While this is close to the situation in many technical applications, the experimental results can only be derived under the assumption of certain models for the description of the sorption process and the conditions (particle shape, material distribution) in the probe material. Furthermore it is not possible to correlate the experimental results with the molecule distribution in the investigated material and hence with certain features of the material leading to the specific sorption behavior observed. An exception from this rule is magnetic resonance imaging [15, 16] which is able to measure the concentration of probe molecules at a certain place in the sample, but the resolution of this technique is still too bad for the

Method	Non-Equilibrium	Equilibrium
macroscopic	Sorption rate IR spectroscopy Frequency response Chromatography ZLC Magnetic resonance imaging	Tracer methods
mesoscopic	IR microscopy	Tracer-IR-microscopy
microscopic	Interference microscopy Coherent QENS	PFG NMR Incoherent QENS

Table 1.1: Summary of experimental techniques applied to study diffusion in porous materials (adopted from [2], p. 2092 and [22], p. 16).

investigation of molecule transport in small crystallites which scale in the micrometer range, while it is sufficient to study this phenomenon on larger scales as for example in bricks or wood [17].

A technique useful for the detection of local concentrations in materials of micrometer scale must at least have a spatial resolution of the same order of magnitude. During the last decade interference and IR-microscopy have been established as experimental techniques that are able to provide such a high resolution [18–21]. With these techniques it is now possible to detect the transient concentration of guest molecules in (transparent) porous materials which makes it possible to directly observe the transport process and to derive the parameters ruling the process without the need of additional model assumptions beside Fick’s laws of diffusion.

1.3 Diffusion Micro Imaging

Micro imaging, the approach to measure guest molecule distributions (profiles!) in host systems by microscopic imaging techniques via uv/vis or infrared microscopy, is a relatively new, not yet commonly used, but nevertheless powerful and promising technique to study mass transport in porous materials.

While most established techniques employed today in order to study mass transport, adsorption and diffusion in porous materials are either batch techniques that get their results by looking on large amounts of material (PFG NMR, ZLC), techniques that concentrate on very small regions in the material (QENS) or techniques that don’t even monitor the transport mechanism itself but draw their conclusions about it by analyzing the self-diffusion

of probe molecules in equilibrium, micro imaging offers a very different - more direct - approach to this topic, as it concentrates on the investigation of transport processes in single crystals via the detection of transient two-dimensional concentration profiles and integral uptake curves. In that way micro imaging techniques avoid averaging over a large number of molecules in different environments (inside and outside the porous material / ambient concentration). Since the evolution of the molecule concentration inside the material is observed directly Fick's laws of diffusion can be used for the analysis of the transport process in their most natural form and without further assumptions and the derived results can directly be correlated to local features of the material morphology, for example transport hindrances on the surface of the material and inside the material itself, again, solely from the interpretation of the concentration profiles.

First attempts to use micro imaging techniques in order to observe mass transport in microporous materials were made by Kärger, Danz and Caro in the early 80's of the 20th century in uptake studies of vapor in zeolite A crystals by using an interference microscope and observing the change of the interference pattern [23], assuming that the observed change of the interference pattern was caused by a change of the refractive index of the crystallite due to the adsorption of water molecules from the surrounding atmosphere. Since the change of the refractive index is the result of guest molecules being adsorbed and not a feature of the molecules itself, it is important to note that it is generally impossible to distinguish between different kinds of guest molecules with interference microscopy.

A systematic approach to sorption studies via interference microscopy was enabled by the work of Schemmert *et al.* [18, 24–26], who developed computer programs and algorithms for data acquisition and the calculation of the probe molecule concentration from the raw data. Schemmert's work was continued over the last decade by a growing number of scientists who devoted their work to a better understanding of diffusion phenomena in numerous studies of transport processes in zeolites and other porous materials [26–36].

Recent advances of the last years concerning interference microscopy were the development of computer software for the analysis of measured concentration profiles and the calculation of the important transport parameters via analytical or numerical methods by Heinke *et al.* [37, 38] and the implementation of a heating system for temperature control during the experiments [39, 40].

For several years interference microscopy [21, 41] has been accompanied by IR microscopy (IRM) as a complementary technique. Compared to interference microscopy IRM has a lower temporal and spatial resolution (Tab. 1.2) which sometimes prohibits the application of IRM due to the relatively small

Technique	Spatial resolution / μm	Temporal resolution / s	Molecule selective
interference microscopy	0.5	10	no
IR microscopy (imaging mode)	2.7	120	yes
IR microscopy (integral mode)	–	0.1	yes

Table 1.2: Summary of the temporal, spatial and chemical resolutions of interference and IR microscopy.

objects that have to be investigated and the extremely short uptake times.

IRM is nevertheless applied to study transport phenomena since it is possible to distinguish between different kinds of molecules with this technique as the molecule concentration inside the material can be derived from the absorption of IR light of a certain wavelength which is specific for one species of guest molecules. It is therefore possible - in contrast to IFM experiments - to study the uptake of mixtures or the progress of a chemical reaction in IRM experiments.

A third application of micro imaging (in relatively poor spatial resolution) was introduced by Han *et al.* who employed confocal laser scanning microscopy to measure concentration profiles in large crystals of the metal organic framework MOF-5 [42]. Contrary to interference and IR microscopy as introduced above, confocal laser scanning microscopy, as employed by Han, does not measure the molecule concentration directly but only the concentration of a reaction product produced in a chemical reaction inside the crystal.

Chapter 2

Methods and Materials

2.1 Interference Microscopy

Interference microscopy, as it was used in this work, is a microscopic technique that enables the observation of mass transport processes in large (several micrometers) and transparent porous materials as crystals or glasses by observing the evolution of molecule concentrations inside the host material.

A generalized illustration of the experimental set-up is given in Fig. 2.1. The material being investigated is put in an optical cell which is placed in the focus of the microscope after the porous material was activated and the cell was evacuated. The pressure system is used to establish the initial pressure p_i in the vacuum system and the optical cell. At the beginning of the experiment the vacuum system is used to change the pressure instantaneously from the initial pressure p_i to the final pressure p_e which can be kept constant for several days during the sorption process. IFM experiments can be carried out at temperatures between room temperature and 100 °C.

Interference microscopy does not measure the molecule concentration inside the investigated materials directly. It rather measures the phase shift of a monochromatic (589 nm) light beam $\Delta\varphi^{(L)}(x, y, t)$ which has passed through the investigated material compared to surrounding of the material as illustrated in Fig. 2.2 [43]. The phase shift is calculated from the interference pattern which is generated inside the microscope by a Mach-Zender type interferometer. The interference pattern can be detected by a CCD camera with a spatial resolution of 512×768 pixels according to a pre-set sequence. With the largest available objective that still has a focal distance that allows the placement of an optical cell under the microscope, each pixel corresponds to an area of $0.5 \mu\text{m} \times 0.5 \mu\text{m}$. The temporal resolution is limited to roughly 10 s due to the exposure times required for suitable signal-to-noise ratios and the applied algorithm used for the calculation of $\Delta\varphi^{(L)}(x, y, t)$ which requires the recording of at least three pictures of the interference pattern

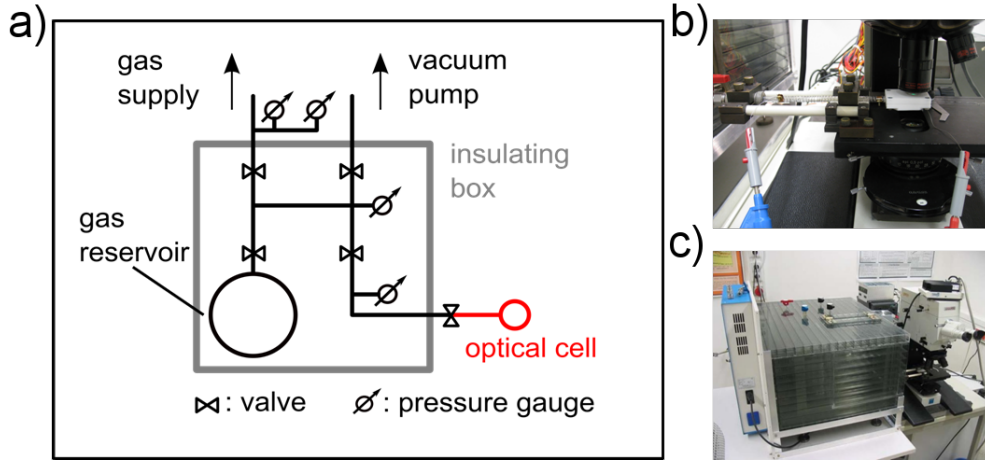


Figure 2.1: Interference and IR microscopy set-up. a) Illustration of the vacuum system. The vacuum system is enclosed by an insulated and heatable box. The sample is placed inside an optical cell which is heated separately and can be connected to the vacuum system (b). c) Insulated box and interference microscope.

for the calculation of one single phase profile [18, 24].

The guest molecule concentration is derived from the phase-profiles by assuming proportionality between the change of the guest molecule concentration and the change of the refractive index of the system consisting of the porous material and the guest molecules at any point in the studied material:

$$\Delta c(x, y, z, t) \propto \Delta n(x, y, z, t). \quad (2.1)$$

The measured phase shift (profile) $\Delta\varphi^{(L)}(x, y, t)$, which will be referred to as the *apparent* concentration (profile) $c_{\text{app}}(x, y, t)$ further on, is the basis for all calculations and results accessible via interference microscopy and is related to the local refractive index and the local concentration by integration in observation direction (z -direction, $L(x, y)$ denotes the thickness of the material in observation direction) since the interference microscope is used in light-transmission mode as follows:

$$c_{\text{app}}(x, y) \equiv \Delta\varphi^{(L)}(x, y) \sim \int_0^{L(x,y)} \Delta n(x, y, z) dz \sim \int_0^{L(x,y)} \Delta c(x, y, z) dz. \quad (2.2)$$

Uptake curves are calculated from the apparent concentration profiles by integrating over the material extension in x - and y -direction (l_x and l_y are the half-length and half-width of the observed material):

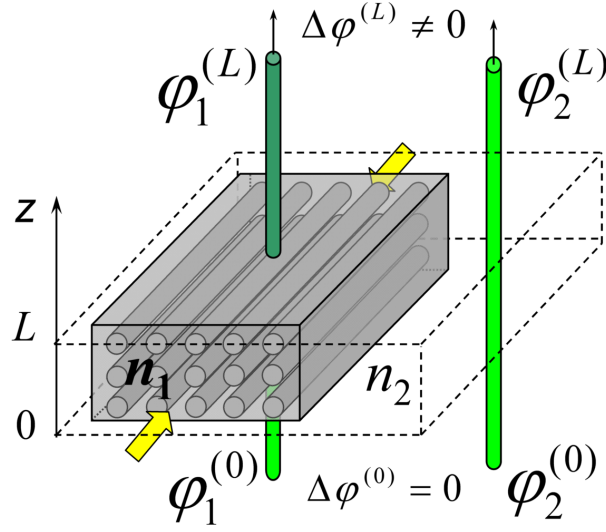


Figure 2.2: Illustration of the situation inside the optical cell. A light beam is split into two parts. One of these parts passes through the investigated material where its phase is shifted according to the refractive index $n(x, y)$ of the host-guest system consisting of porous material and guest molecules. IFM measures the phase difference $\Delta\varphi^{(L)}(x, y, t) = \varphi_1^{(L)}(x, y, t) - \varphi_2^{(L)}(x, y, t)$ between both parts of the light beam from which the apparent guest molecule concentration inside the material is calculated.

$$m(t) = \int_{-l_x}^{l_x} \int_{-l_y}^{l_y} c_{\text{app}}(x, y, t) \, dy \, dx \quad (2.3)$$

This way of data acquisition makes it usually quite complicated - but not impossible - to investigate uptake in observation direction. Interference microscopy is in fact better used to investigate transport processes in materials in which the transport process is one- or two-dimensional, e.g. materials with one- or two-dimensional pore systems that can be arranged perpendicular to the observation direction. In that case the local concentration becomes a function of x and y only and the integral in Eq. 2.2 vanishes, leading to Eq. 2.4:

$$c_{\text{app}}(x, y, t) = L(x, y) \cdot c(x, y, t). \quad (2.4)$$

The most convenient material - from the point of data analysis - is a material with parallel surfaces (that means constant thickness L) in observation direction (which is often the case for large single crystals which often can be synthesized in well defined geometric shapes, e.g. cubes). In that case the measured apparent concentration becomes directly proportional to the local concentration inside the material (Eq. 2.5).

$$c_{\text{app}}(x, y, t) = L \cdot c(x, y, t). \quad (2.5)$$

As interference microscopy is not able to measure the concentration inside the host material quantitatively, the measured data has to be calibrated. This is usually done by comparing the measured isotherms with data from the literature or from computer simulations. A commonly observed isotherm shape in microporous materials is the so called Langmuir isotherm (Eq. 2.6) which describes the correlation between pressure p and concentration $c(p)$ by only two parameters, the maximum concentration c_{eq} possible and the parameter k_L :

$$c(p) = c_{\text{eq}} \cdot \frac{k_L p}{1 + k_L p}. \quad (2.6)$$

2.2 Porous Materials

2.2.1 General

Porous materials cover a wide range of solid organic and inorganic materials that share one common feature: They consist of voids surrounded (or defined) by a solid and impenetrable matrix. Prominent and widely known members of this material class are wood, concrete, fungi and bird bones. Packed beds of solids might also be interpreted as porous materials.

One way to categorize these materials is by the size of their voids (pores). According to the classification of the International Union of Pure and Applied Chemistry (IUPAC), materials with pore diameters below 2 nm are referred to as *micro*-porous materials, materials with pore diameters between 2 nm and 50 nm are called *meso*-porous materials and materials with larger pores are *macro*-porous [44].

Materials with micro- and meso-pores possess many features which make them interesting for industrial processes [45, 46]. They are employed as sieves on molecular length scales in separation and refinement processes in oil industry [47, 48]. Their large internal surface makes them excellent devices for fluid storage via adsorption on this surface, which is of interest for hydrogen storage or nitrogen deposition. And they are also used as matrix materials for the equal distribution of catalytic centers in their pore space, making some porous materials important role players in catalysis [49]. In many of these applications mass transport plays an important role and transport properties may decide if a material is used in a certain process or not, making the investigation of transport processes in these materials useful and important.

In this work, mass transport was studied in single crystals of microporous zeolites (the most commonly used microporous material) and metal organic frameworks (MOFs, a promising new group of porous materials) which shall now be described in a more detailed manner.

2.2.2 Zeolites

Zeolites were first described in the literature by Friedrich Axel Cronstedt in 1756 [50]. Cronstedt observed that when heated, zeolites would release hot liquid and steam as if they were boiling (Greek: *zeo lithos*, boiling stone). With his experiments he already discovered the property of zeolites that makes them interesting for technical applications and that is still (e.g. in this work) in the focus of scientific investigation: Zeolites are able to store (adsorb) and release (desorb) substantial amounts of fluids - for example water or small hydrocarbons - according to the conditions in their surrounding.

In nature, zeolites rarely occur in pure and uncontaminated form as they often contain varying degrees of other minerals, metals, quartz, or other zeolites. It is therefore often simply not possible to use naturally occurring zeolites in commercial applications where uniformity and purity are important. First successful attempts to produce synthetic zeolites are reported in the 1950's and 1960's by Barrer and Milton [51]. From that time on, a large number (about 190 in 2012) of different zeolite structures (framework types) have been reported and characterized [52].

The basic feature all zeolite structures have in common is their chemical composition of silicon- and aluminum-oxide complexes, which form the three-dimensional crystal network that defines the pore structure of the certain zeolite. Depending on the given ratio of aluminum and silicon, the network might be charged. The negative charge is balanced by counterions (Na^+ or Ca^{2+}) which are located in the cavities of the pore network and which therefore might influence the sorption behavior of the material. The synthesis of the same framework type with a different chemical composition - in pure silicon form, which is uncharged and free of cations in the framework, in AlPO form, which is also free of cations, or a material in which the aluminum is replaced by an other metal atom e.g. boron - can therefore lead to unexpected effects in the performance of the material.

2.2.3 Metal-Organic Framework – MOFs

Metal-organic frameworks, also called 'coordination polymers' or 'metal-organic coordination networks' (MOCNs) are a novel class of microporous materials. Their framework is built of two central components, the connec-

tors (metal ions or clusters) and the linkers (organic ligands) which link the metal clusters. The features of the pore network (dimension, pore size) are determined by the linker-connector pair chosen for the synthesis. The synthesis of MOFs is a challenging task since many combinations of connector and linker will lead to unstable or useless materials due to the creation of too large pores or unexpected connections, which block pores so that the first stable MOF materials were not reported until the end of the 20th century.

The pore networks of MOFs - that means the pore sizes and the accessible pore volumes - can be made very similar to those of zeolites (there even exist MOFs that have a pore structure identical to that of zeolites but on a different length scale due to the deviating size of the linker used in the MOFs), but the main advantage of these materials is indeed the option to tailor the pores by using different linkers or connectors. In contrast to zeolites which have a quite rigid crystal structure, MOF structures are more flexible. That means that the presence of guest molecules can influence the shape of the pore network, e.g. the pore diameter or diameter of windows (*breathing* or *gate opening* effect [53]), connecting adjacent cavities, which might have an important influence on the transport behavior of the material.

2.3 Diffusion and Mass Transport

2.3.1 Diffusion Basics

Diffusion in general is an omnipresent, but often overlooked phenomenon in our daily lives: Traffic - can be described by diffusion! The propagation of certain genetic characteristics, languages and ideas - it's diffusion! The distribution of minerals in the core of the earth or of impurities in semiconductors - also diffusion! The arrangement of products and shelves in supermarkets - not diffusion itself, but derived from diffusion experiments under consideration of how to lead the customers to a certain place in the market and how to keep him there via diffusion barriers. And finally going back to the roots of diffusion measurements: The random movement of particles (pollen on water, drunken men on the streets and, quite in general, all molecules) due to their thermal energy [54].

In order to describe diffusion in a physical (mathematical) way, it is useful to distinguish between diffusion processes under equilibrium conditions, conditions under which no mass transport occurs and under which the particles move only randomly due to their thermal energy, and non-equilibrium conditions under which the particle motion follows the gradient of a physical quantity (pressure/chemical potential) in its surrounding.

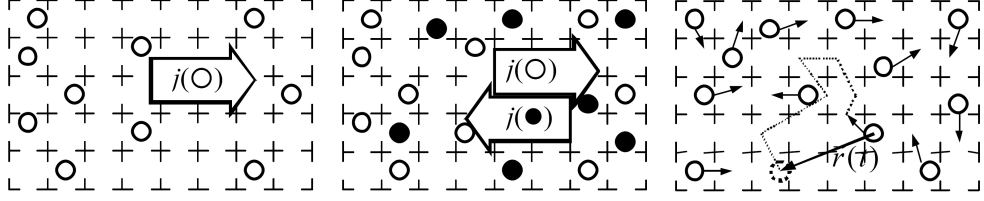


Figure 2.3: Illustration of three different kinds of diffusion: The directed motion of particles under non-equilibrium conditions (transport diffusion, *left*), the directed motion of marked particles under equilibrium conditions (tracer exchange diffusion, *middle*) and random motion of unmarked particles under equilibrium conditions (self-diffusion, *right*) [5].

Under equilibrium conditions the motion of the diffusing particles is described by the famous Einstein relation (Eq. 2.7) which correlates the mean square displacement $\langle \vec{x}^2 \rangle$ of a particle diffusing in d dimensions with the diffusion time t via the self-diffusion coefficient D_s of the particle (see the *right* part of Fig. 2.3) [55].

$$D_s = \frac{\langle \vec{x}^2 \rangle}{2dt} \quad (2.7)$$

For diffusion under non-equilibrium conditions the existence of a flux \vec{j} , the net amount of particles (molecules) that cross the area A per time t (see *left* part of Fig. 2.3), is characteristic [56]. This flux occurs due to an external force, which is, according to Fick's 1st law, the gradient $\vec{\nabla}c$ of the local molecule concentration. The coefficient correlating both quantities is called the transport-diffusion coefficient D .

$$\vec{j} = -D\vec{\nabla}c \quad (2.8)$$

The local concentration c will change due to the flux \vec{j} . The temporal evolution of the particle concentration is described by Fick's 2nd law (Eq. 2.10) which can be derived by combining Eq. 2.8 with the law of conservation of matter Eq. 2.9.

$$\vec{\nabla}\vec{j} + \frac{\partial c}{\partial t} = 0 \quad (2.9)$$

$$\frac{\partial c}{\partial t} = \vec{\nabla}(D\vec{\nabla}c) \quad (2.10)$$

If the diffusivity does not depend on the local particle concentration Eq. 2.10 reduces to Eq. 2.11. However, there is strong experimental evidence that in many cases the transport diffusivity does depend on concentration.

$$\frac{\partial c}{\partial t} = D\Delta c \quad (2.11)$$

A diffusion hybrid in some way is the so called tracer-exchange diffusion which is illustrated in the *center* part of Fig. 2.3. Here the self-diffusion of marked particles can be analyzed with methods usually used for the description of transport diffusion (that means the analysis of concentration profiles). The experiment is carried out under equilibrium conditions, except that some molecules are marked at the beginning of the experiment so that the flux of these molecules can be detected over time while the net flux, the sum of the fluxes of marked and unmarked molecules, is still zero as expected under equilibrium conditions. In experiments this scenario can be realized for example by monitoring the diffusion of deuterated molecules in a porous material, previously saturated with non-deuterated molecules of the same species, by IR microscopy [41, 57].

2.3.2 Diffusion in Porous Materials

In this work, mass transport was studied on microporous zeolite and MOF crystals. The pore system of these materials is geometrically ordered and composed of channels, cavities and windows over which cavities are connected – a highly restrictive environment for the probe molecules to diffuse in as they often are of a size comparable to the pore diameters. Diffusivities measured in porous materials can therefore be significantly different (lower) from diffusivities measured in bulk phase.

Self-diffusion and transport-diffusion in porous materials are not necessarily unrelated. A good estimation of the self-diffusivity can be achieved by describing mass transport not in the fickian way but in the thermodynamic invariant way. The thermodynamic invariant corrected diffusivity D_0 is related to the self-diffusivity by Eq. 2.12 [5, 58]. If the interaction of the guest molecules is negligible, which is often the case for microporous materials in which the molecules diffuse in cavities which are separated by narrow windows, the particle-particle interaction term D_{pp} can be ignored and the corrected diffusivity becomes equal to the self-diffusivity.

$$\frac{1}{D_s} = \frac{1}{D_0} + \frac{\theta}{D_{pp}} \approx \frac{1}{D_0} \quad (2.12)$$

The corrected diffusivity and transport diffusivity D are correlated via the thermodynamical factor $\Gamma = \partial p / \partial c$ (which can be derived from the sorption isotherm (e.g. Eq. 2.6)) by Darken's relation [58]:

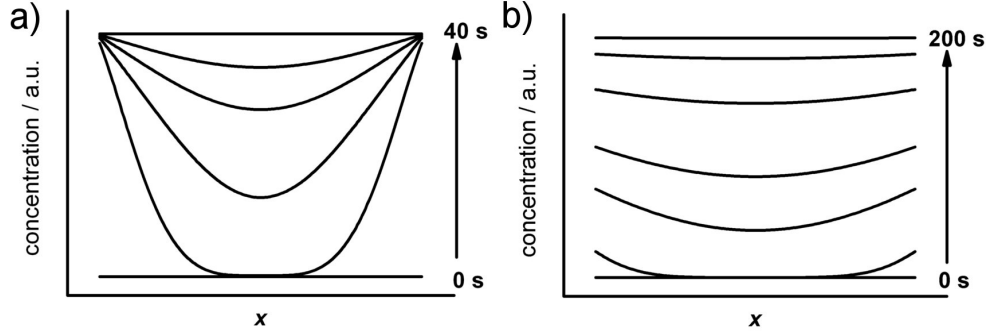


Figure 2.4: Influence of surface barriers on mass transport. Simulated concentration profiles of a one-dimensional uptake process for a high (a) and low (b) surface permeability. The decelerating influence of the surface barrier is easily visible in the shape of the profiles and the time scale of the uptake process.

$$D = D_0 \cdot \frac{\partial \ln p}{\partial \ln c} = D_0 \cdot \Gamma. \quad (2.13)$$

If the sorption isotherm is of single-site Langmuir type (Eq. 2.6), the thermodynamic factor can be calculated analytically:

$$\Gamma = (1 + c/c_{\text{eq}}) \quad (2.14)$$

In sorption experiments with nanoporous materials, it was frequently observed that the transport process is retarded at the surface of the material. This effect can be taken into account by introducing a second quantity, the surface permeability α according to Eq. 2.15 for each material surface:

$$j = \alpha(c_{\text{surf}}(t = \infty) - c_{\text{surf}}(t)). \quad (2.15)$$

The influence of surface barriers is illustrated in Fig. 2.4. Figure 2.4a shows simulated one-dimensional concentration profiles with negligibly small surface barriers. In this case the concentration at the surface c_{surf} almost instantaneously approaches the equilibrium concentration $c_{\text{eq}} = c(t = \infty)$. The opposite case is illustrated in Fig. 2.4b. Here the surface concentration increases only slowly with time, altering the shape of the concentration profiles and the time scale of the uptake process. Profiles as shown in Fig. 2.4 are used to derive the transport diffusivity and surface permeability from them by applying Fick's equations or fitting experimentally obtained profiles with simulated ones.

While the diffusion process is more or less understood in porous materials, the nature and even the existence of surface barriers is still under

discussion [59–63], although the permeation step is of crucial importance for the transport process ('no permeation, no uptake' so to say).

2.3.3 Temperature Effects

The set of parameters employed in this work in order to describe the observed transport processes (transport parameters) is completed by the activation energies for diffusion and surface permeation $E_{A,\text{diff}}$ and $E_{A,\text{perm}}$. These energies can be derived via Eq. 2.16 if Arrhenius-like behavior is observed.

$$D(T) = D(T = \infty) \cdot \exp\left(-\frac{E_A}{RT}\right). \quad (2.16)$$

Although this method has been used to determine the activation energies for diffusion and for surface permeation, there might be host-guest systems where this approach is not feasible.

2.4 Data Analysis

2.4.1 Integral Uptake Curves

The experimental data available to IFM during the sorption process are either two-dimensional profiles of the integrated guest molecule concentration $c_{\text{app}}(x, y, t)$ in the plane perpendicular to the observation direction or integral uptake curves $m(t)$ (see Eq. 2.2 and Eq. 2.3) which can be analyzed in order to derive the relevant transport parameters.

While the concentration profiles naturally contain more information in greater detail than integral uptake curves – especially on the location of transport barriers and the concentration dependence of the transport parameters, it is often much easier, faster and in many cases sufficient and simply more convenient to analyze uptake curves, especially in the case of IR experiments which have a poor temporal and spatial resolution in imaging mode but an excellent temporal resolution if used in integral mode. The analysis of uptake curves is usually done by fitting the measured data with the appropriate analytical solution corresponding to the geometry of the studied material and its pore network. Solutions are available in the literature for various geometrical structures for solely diffusion controlled uptake and also for uptake processes retarded by surface barriers [64]. However, by introducing α as a second fit parameter usually the accuracy of the fit is increased, but the accuracy of the determined transport parameters is decreased. For this reason transport parameters presented in this work which were calculated from uptake curves have been derived using models for diffusion controlled uptake only.

Equation 2.17 gives an example for an analytical solution for uptake, here in a cube of half-edge length l :

$$1 + \frac{512}{\pi^6} \sum_{k,m,n=1}^{\infty} \frac{\frac{m(t)}{m(t=\infty)} = \exp(-\frac{\pi^2 D t}{4l^2} ((2k-1)^2 + (2m-1)^2 + (2n-1)^2))}{(2k-1)^2 (2m-1)^2 (2n-1)^2} \quad (2.17)$$

The most serious drawback of working solely with uptake curves when determining transport parameters is that all available analytical solutions are derived for constant diffusivities and permeabilities. As transport diffusivity and surface permeability often *do* depend on concentration it is necessary to follow the uptake in several small-step adsorption or desorption experiments in which the relative concentration change is small compared to the equilibrium loading. For data analysis each of these experiments can afterwards be treated as if the transport parameters are constant without creating large errors. The concentration dependence is achieved by plotting the results of each small-step experiment versus the mean concentration present during the experiment.

2.4.2 1d Concentration Profiles

The analysis of transient concentration profiles can be done in many different ways, depending on the number of dimensions the transport process takes place in and on the quality of the profiles. If the uptake process is one-dimensional, methods relying on Fick's 1st and 2nd law (Eq. 2.8, 2.10) can be applied to determine the diffusivity. The surface permeability can be determined via Eq. 2.15 if the flux into the material through one surface is calculated by integrating the one-dimensional concentration profile from the edge to the center [37].

If surface barriers are negligibly small ($c(t) = c(t = \infty), t > 0$), subsequent concentration profiles will coincide with each other if plotted versus x/\sqrt{t} rather than x and if the diffusion fronts have not yet reached the center of the material. In that case the transport diffusivity can be determined via the Boltzmann–Matano method (Eq.2.18) from the one-dimensional profile $c(x)$ at time t :

$$D(c) = -\frac{1}{2t} \frac{dx}{dc} \int_{c=c_{\text{start}}}^c x \, dc, \quad (c_{\text{start}} < c < c_{\text{eq}}). \quad (2.18)$$

With this method the complete information about the concentration dependent diffusivity in the whole concentration range covered in the experiment is extracted from only one concentration profile, making the Boltzmann–

Matano method a powerful and elegant tool for the analysis of mass transport.

2.4.3 2d and 3d Profiles

A less elegant but also very powerful – since more general – method for the analysis of transient concentration profiles is the fitting algorithm based on a finite difference solution of Fick’s laws under consideration of surface barriers as boundary condition introduced by *Heinke et al.* in [37, 38]. This method can be applied for the analysis of one-, two- and three-dimensional uptake processes and will derive the transport diffusivity and surface permeabilities as function of the covered concentration range.

$D(c)$ and $\alpha(c)$ are used as fit parameters while comparing profiles simulated with the supposed $D(c)$ and $\alpha(c)$ functions with the measured profiles via χ^2 calculations. The concentration dependence of $D(c)$ and $\alpha(c)$ is altered independently in each simulation run. The best fit between simulated and measured profiles is supposed to give the best approximation of surface permeability and diffusivity.

2.4.4 Accuracy of Diffusivity and Permeability Data

The diffusivity and surface permeability data presented in this work have been calculated based on experimentally measured concentration profiles applying the fitting procedure described in the previous sections.

In general, the accuracy of those fits is limited by:

- (i) the quality of the measured concentration profiles (noise)
- (ii) the amount of available computation time (number of fitting runs, number of free parameters to describe the concentration dependence of D and α).

Reasonable fitting procedures result in mean deviations between the measured and calculated profiles of less than 5%. Depending on the quality of the profiles and the number of free parameters the deviation might be decreased below 2%.

The error of the calculated transport parameters can be estimated by varying each fitting parameter individually until the accuracy of the fit decreases by 1% in comparison to the best possible fit. Experience has shown that a deviation of 1% in the accuracy of the fit from the best possible fit may correspond to a change of about 30% in the diffusivity and permeability values for one single crystal.

2.5 Observation Window

For each experimental technique the size of the observation window, which is in the case of interference microscopy the range of diffusivities and surface permeabilities that can be observed, has to be determined. While this has already been discussed by Schemmert in [25] for the observable diffusivity range, no estimation has been made for the surface permeabilities, probably due to the lack of knowledge about their actual size and their importance for mass transport in real porous systems.

Obviously the range of observability is restricted by the temporal and spatial resolution of the microscope. From experimental experience crystals with half edge length of roughly 10 μm are necessary to obtain concentration profiles of sufficiently good resolution. The first profile can, due to restrictions of the set-up, be obtained roughly 15 seconds after the start of the experiment. In order to estimate an upper limit for detectable surface permeabilities I make the following assumptions and use the following short cuts:

1. Three-dimensional uptake is faster than two-dimensional uptake which is again faster than one-dimensional uptake. I will therefore concentrate on 3d systems for my estimation, since they make the highest demands on the spatial resolution. An upper limit for 3d systems is also an upper limit for 2d and 1d systems.

2. For reasons of simplicity I will use the solution of Fick's law for a cubic isotropic structure (edge length $2l$) and constant diffusivities and permeabilities, integrated in z -direction which simulates the situation found in IFM experiments, for my estimation:

$$\frac{c_{\text{app}}(x, y, t)}{c_{\text{app}}(x, y, t = \infty)} = 1 - \sum_{n_x, n_y, n_z=1}^{\infty} \frac{2B \exp(-\beta_{n_x}^2 Dt/l^2) \cos(\beta_{n_x} x/l)}{(\beta_{n_x}^2 + B^2 + B) \cos(\beta_{n_x})} \times \frac{2B \exp(-\beta_{n_y}^2 Dt/l^2) \cos(\beta_{n_y} y/l)}{(\beta_{n_y}^2 + B^2 + B) \cos(\beta_{n_y})} \times \frac{2B^2 \exp(-\beta_{n_z}^2 Dt/l^2)}{(\beta_{n_z}^2 + B^2 + B) \beta_{n_z}^2} \quad (2.19)$$

where β_n is the n th root of

$$\beta \tan(\beta) = B = \frac{\alpha l}{D} = \frac{\alpha/l}{D/l^2} \quad (2.20)$$

3. For the calculation of the surface concentration I will focus on a point in the middle of one of the crystal edges ($x = 0, y = l$) since here the lowest surface concentration is measured if everything is symmetric as expected.

4. I will neglect all but the first part of the sum in Eq. 2.19. Although this would underestimate the surface concentration in general, the error is quite small since the summands in Eq. 2.19 decay quickly. This error and uncertainties (noise) of the measured concentration profiles are taken into account by postulating that the surface concentration at $x = 0$ and $y = l$ calculated via Eq. 2.19 for the first profile at 15 s must be lower than 95 % of the equilibrium concentration $c_{\text{app}}(x, y, t = \infty)$ in order to allow the reliable detection of the surface barrier.

5. I will concentrate on uptake processes that are controlled by the surface barrier (high diffusivity and low α lead to flat profiles; for example $B \leq 0.1$). In that case the estimation will also be correct for lower diffusivities (slower uptake) and Eq. 2.19 will simplify significantly: If $B \leq 0.1$, $\tan(\beta) \approx \beta$ and Eq. 2.20 simplifies to $B \approx \beta^2$. For this rough estimation it is also sufficient to assume that $\cos(\beta) \approx 1$ without losing further accuracy.

With this assumptions the surface concentration at $x = 0$ and $y = l$ according to Eq. 2.19 is

$$c_{\text{surf}}(\alpha, l, t) \simeq 1 - \left(\exp\left(-\frac{3\alpha}{l}t\right)\right) \quad (2.21)$$

which might be written more generally for d -dimensional uptake as

$$c_{\text{surf}}(\alpha, l, t) \simeq 1 - \left(\exp\left(-\frac{d\alpha}{l}t\right)\right). \quad (2.22)$$

Rearranging Eq. 2.22 gives the following estimation for the maximum surface permeability α_{max} detectable by interference microscopy:

$$\alpha_{\text{max}} = \frac{l}{dt} \cdot \ln 20. \quad (2.23)$$

Finally α_{max} can be estimated for $t = 15$ s and $l = 10$ μm by:

$$\alpha_{\text{max}} \approx \frac{2}{d} \cdot 10^{-6} \frac{m}{s}. \quad (2.24)$$

Chapter 3

MOF Zn(tbip)

3.1 Material Description

Zn(tbip) ($H_2tbip = 5\text{-tert-Butyl Isophthalic Acid}$) is a highly stable representative of the family of microporous metal organic frameworks (MOFs, see section 2.2.3). The crystals are elongated, hexagonally prismatic crystallites with lengths of hundreds and diameters of tens of micrometers. Typical examples for the specimens applied in the experiments are shown in Fig. 3.1a. A detailed description of the synthesis, the chemical composition and the characteristics of Zn(tbip) can also be found in [65].

Important for mass transport purposes, the crystals are traversed by one-dimensional pores which run along the longitudinal axis of the crystallites (Fig. 3.1). The accessible pore space, illustrated in Fig. 3.1c, is formed by cavities of petal-like shape with maximum diameters of 1.44 nm and a separation of 0.82 nm. The cavities are connected through narrow windows of 0.45 nm diameter in a way that the unit cell is formed by six of these cavities. The narrow windows do not allow more than one molecule to traverse through a certain window at the same time, making the material a candidate for the scientifically interesting phenomenon of single-file diffusion [66–68], a special kind of diffusion in which a molecule can only move if the final position and the whole path to that point are not occupied by other molecules.

3.2 Diffusion and Surface Permeation in Zn(tbip)

The mass transport of small hydrocarbons (ethane, propane and n-butane) in Zn(tbip) at room temperature was investigated thoroughly by Tzoulaki *et al.* and Chmelik *et al.* with interference and IR microscopy as reported in [35, 38, 69] with the following results: If D is plotted as a function of c and α is plotted as a function of the mean concentration $c_{\text{mean}} = (c + c_{\text{eq}})/2$, the

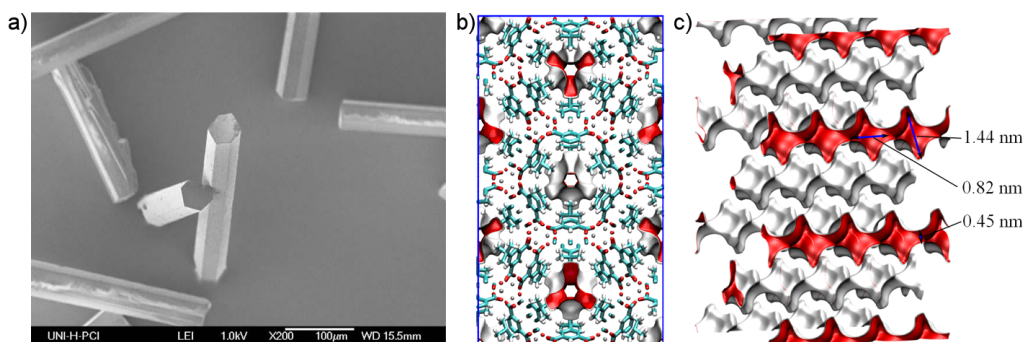


Figure 3.1: Metal organic framework (MOF) Zn(tbip). a) SEM picture of Zn(tbip) crystals as used in the experiments. The one-dimensional pores run along the longitudinal axis of the crystals. b) View in channel direction illustrating the small window aperture of 0.45 nm comparable to the kinetic diameter of most small hydrocarbons. c) Pore system in Zn(tbip). The pores are illustrated by areas of identical energy as seen from the molecules in the channels (*red*).

ratio $\alpha(c_{\text{mean}})/D(c)$ was basically invariant (i) for the studied molecules (ii) under both, non-equilibrium (uptake experiments) and equilibrium (tracer-exchange experiments [35]) conditions (iii) over the observed loading range. This finding is in contrast to the conventional picture of transport resistances at phase boundaries as homogeneous layers of dramatically reduced diffusivities (or solubilities) with properties notably different from those of the bulk phase and indicates therefore that surface permeation and intra-crystalline diffusion in Zn(tbip) are evidently controlled by *the same* mechanism!

Deeper insights into the origin of the proposed mechanism that controls surface permeation and diffusion in Zn(tbip) crystals might be achieved by measurements at different temperatures and the calculation of activation energies for diffusion and surface permeation. If the mechanism really is the same, the activation energies also should be the same. So far practical restrictions of the IRM and IFM set-ups have prohibited transient uptake and release experiments at different temperatures. Recent improvements on the experimental system (Fig. 2.1) have helped to overcome this limitation and the measurement of transient concentration profiles is no longer limited to room temperature.

The experimental results with propane obtained at elevated temperatures of 323 K and 343 K are summarized in Fig. 3.2. In a first step the measured profiles from several uptake experiments on two different crystals were calibrated by comparing the measured equilibrium loadings with the isotherm given in [38]. After the loading was known quantitatively at room temperature, the loading at 323 K and 343 K could be estimated by comparing

the apparent equilibrium concentrations measured at the given temperatures with each other. For all three temperatures Langmuir isotherms (Eq. 2.6) were assumed as it was done in [38] for room temperature (Fig. 3.2a). The Langmuir parameters $k_L(T)$ at temperature T were calculated to $k_L(295 \text{ K}) = 0.015 \text{ mbar}^{-1}$, $k_L(323 \text{ K}) = 0.0044 \text{ mbar}^{-1}$ and $k_L(343 \text{ K}) = 0.0027 \text{ mbar}^{-1}$. After calibration, the concentration profiles along channel direction were fitted with the computer algorithm explained in section 2.4. The transport parameters were calculated using the Reed-Ehrlich model [70] in the same way as it was applied in [38].

Transport diffusivity and surface permeability are plotted in Fig. 3.2b for the experimentally covered loading range and in Fig. 3.2c for zero loading. Both quantities show identical temperature and concentration dependencies, and therefore identical activation energies (Fig. 3.2c). The difference in the permeability/diffusivity ratios of the two crystals may be taken as an indication of different realizations of the surface blockages, while the similarity of the Arrhenius slopes confirms that surface permeation and bulk diffusion proceed by identical elementary mechanisms.

3.3 A Model for Surface Permeation and Diffusion in Zn(tbip)

In conventional transport models, diffusivity and surface permeability are controlled by different (and generally independent) mechanisms and vary independently of each other which was so far also the overall outcome of previous studies dealing with this topic [32, 71]. A common barrier model is illustrated in Fig. 3.5. The transport barrier is considered to be a thin layer of thickness l and reduced diffusivity D_{barr} which might be explained by changes in the lattice properties close to the surface. In that case Fick's 1st law (Eq. 2.8) may be written as

$$j(x=0) = D_{\text{barr}} \frac{c_{\text{eq}} - c(x=0)}{l} \quad (3.1)$$

which yields, if compared with the definition of the surface permeability Eq. 2.15:

$$\alpha = D_{\text{barr}}/l. \quad (3.2)$$

Alternatively, and completely equivalently with the above model, transport inhibition may also result from a dramatic reduction of guest solubility. Then D_{barr} is replaced by the bulk diffusivity reduced by the ratio of the concentrations in the bulk and in the layer at equilibrium. However, the experimental

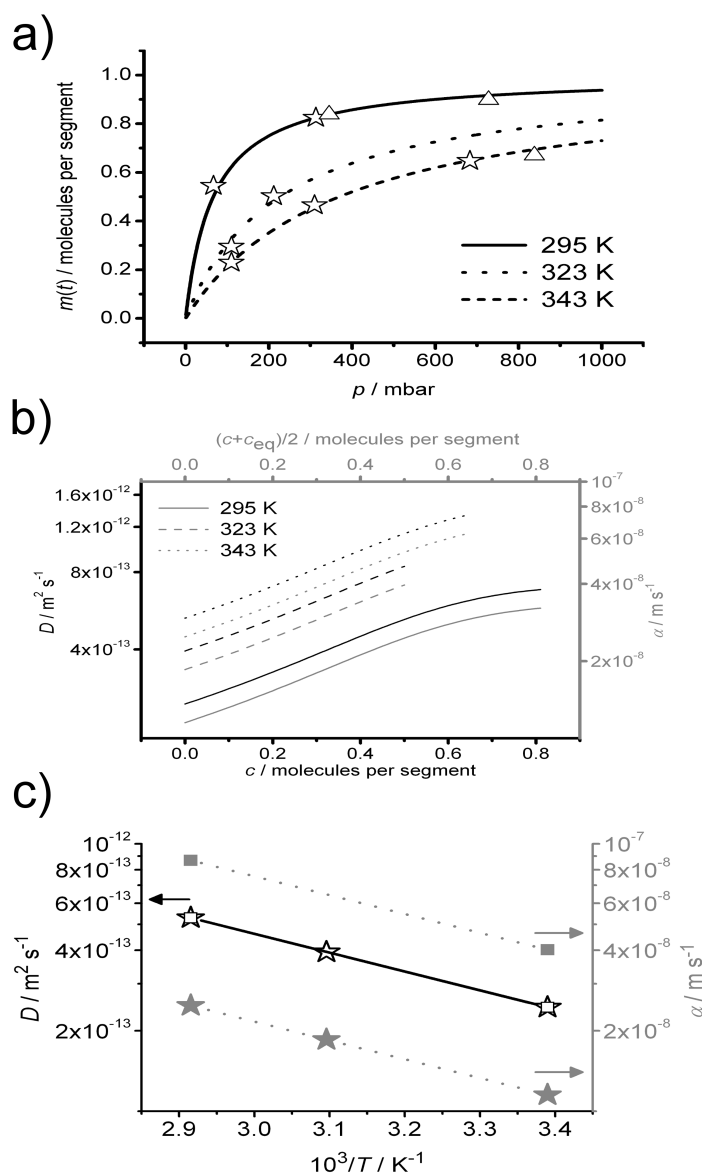


Figure 3.2: Mass transport of propane in Zn(tbip) at elevated temperatures. a) Fitted single-site-Langmuir isotherms for propane uptake at 295 K (full line), 323 K (dotted line) and 343 K (dashed line). The isotherm at 295 K is taken from [38]. It is matched well by the results observed with two different crystals (triangle, star) used for the experiments at elevated temperatures. b) Concentration dependence of diffusivities and surface permeabilities, similar at 295 K, 323 K and 343 K. For concentration profiles and simulation results see Figs. 3.4 and 3.3. c) Temperature dependence of diffusivity and surface permeability. Surface permeability (filled symbols) and intra-crystalline diffusivity (open symbols) of propane in MOF Zn(tbip) at vanishing loading at different temperatures, determined from the transient concentration profiles recorded in two different crystals (stars, squares, see Figs. 3.4 and 3.3) during molecular uptake by interference microscopy (IFM).

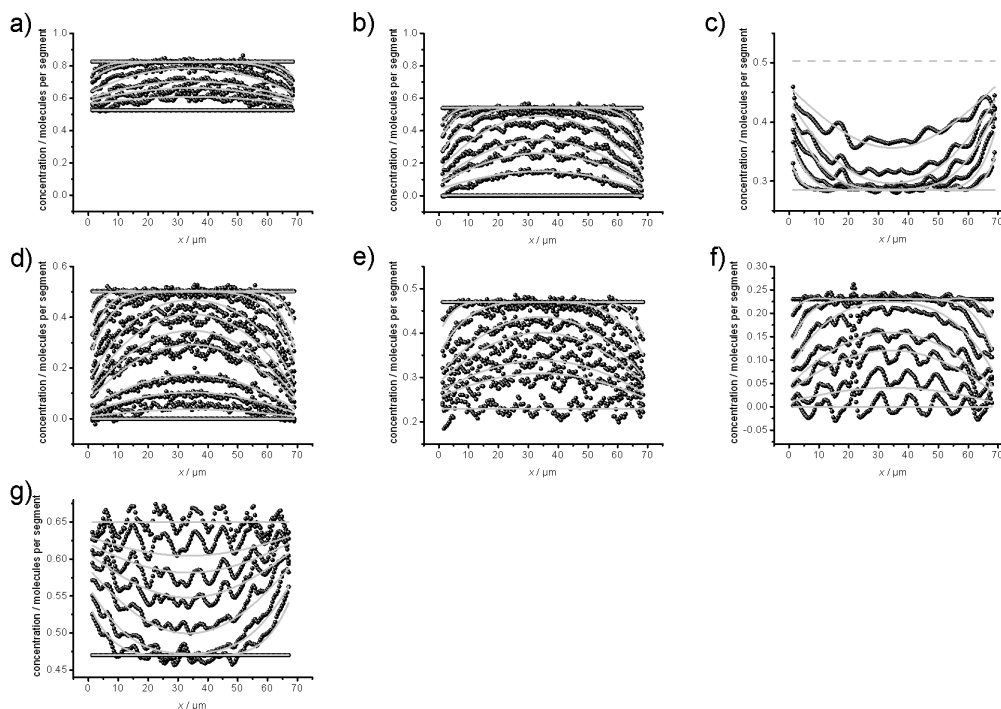


Figure 3.3: Concentration profiles for propane in the first studied crystal. a) Desorption profiles for a pressure step 313–67 mbar propane at 295 K (from top to bottom: $t/s = 0, 30, 110, 470, 1470, 3470, 19670, \infty$). b) Desorption profiles for a pressure step 67–0 mbar propane at 295 K (from top to bottom: $t/s = 0, 30, 130, 570, 1470, 3470, 7970, 19970, \infty$). c) Adsorption profiles for a pressure step from 100 mbar to 211 mbar propane at 323 K (from bottom to top: $t/s = 0, 10, 70, 170, 470, 1470, \infty$). d) Desorption profiles for a pressure step 211–0 mbar propane at 323 K (from top to bottom: $t/s = 0, 10, 70, 170, 470, 770, 1470, 1970, 7970, 28970, 43970, \infty$). e) Desorption profiles for a pressure step 309–110 mbar propane at 343 K (from top to bottom: $t/s = 0, 10, 110, 370, 770, 1470, 3470, \infty$). f) Desorption profiles for a pressure step 110–0 mbar propane at 343 K (from top to bottom: $t/s = 0, 10, 70, 270, 770, 1470, 7970, \infty$). g) Adsorption profiles for a pressure step 313–638 mbar propane at 343 K (from bottom to top: $t/s = 0, 30, 90, 270, 570, 1470, 7970, \infty$).

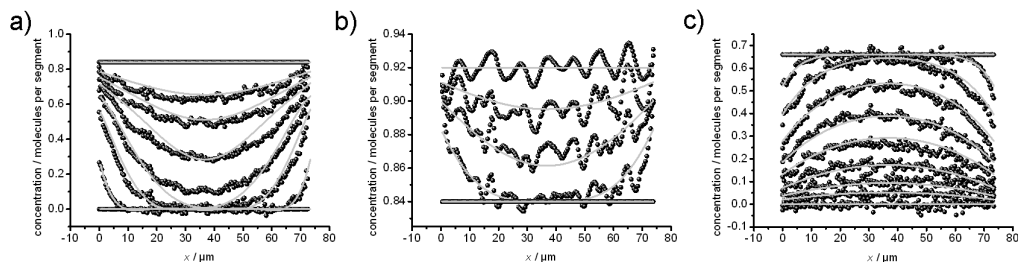


Figure 3.4: Concentration profiles for propane at different temperatures in the second studied crystal. a) Adsorption profiles for a pressure step 0–350 mbar propane at 295 K (from bottom to top: $t/s = 0, 10, 170, 470, 970, 7970, \infty$). b) Adsorption profiles for a pressure step 350–768 mbar propane at 295 K (from bottom to top: $t/s = 0, 30, 270, 4970, \infty$). c) Desorption profiles for a pressure step 838–0 mbar propane at 343 K (from top to bottom: $t/s = 0, 10, 50, 170, 370, 770, 3470, 10970, 34970, \infty$).

results can not be explained sufficiently by such a model, as deviations in the α/D ratio or in the concentration dependence would be expected - at least for different molecules. Since this is not the case, an alternative model must be proposed.

In 2005, Dudko *et al.* published the results of Monte-Carlo diffusion simulations in a geometry illustrated in Fig. 3.6a: cubes of edge length L are interconnected in all directions by holes of diameter $2a$ (see Fig. 3.6a) [72]. In their work Dudko and co-workers show that the permeability of a given plane in this geometry is proportional to the diffusivity. A behavior as observed in the experiments with Zn(tbip):

$$\alpha = 2a/L^2D \quad (3.3)$$

Inspired by Dudko’s approach, Heinke modified the geometry in order to make it more similar to the pore space of Zn(tbip) (Fig. Fig. 3.6b). In his model diffusion takes place in one-dimensional channels with a diameter equal to that of the probe molecules that were used in the simulation. Theoretically this would allow only single-file diffusion as it was expected for Zn(tbip), but not observed during the experiments [35]. Heinke considers the experimental results by randomly distributing interconnections in y - and z -direction between adjacent channels with a probability of p . At these intersections the probe molecules can exchange between the connected channels. A known reason for such interconnection in real crystals are defects in the crystal structure at which the lattice might be shifted in a way that creates new connection [73]. The transport barrier at the surface - and this is the main concept of the model - is realized by the total blockage of pore entrances for mass transport at the surface.

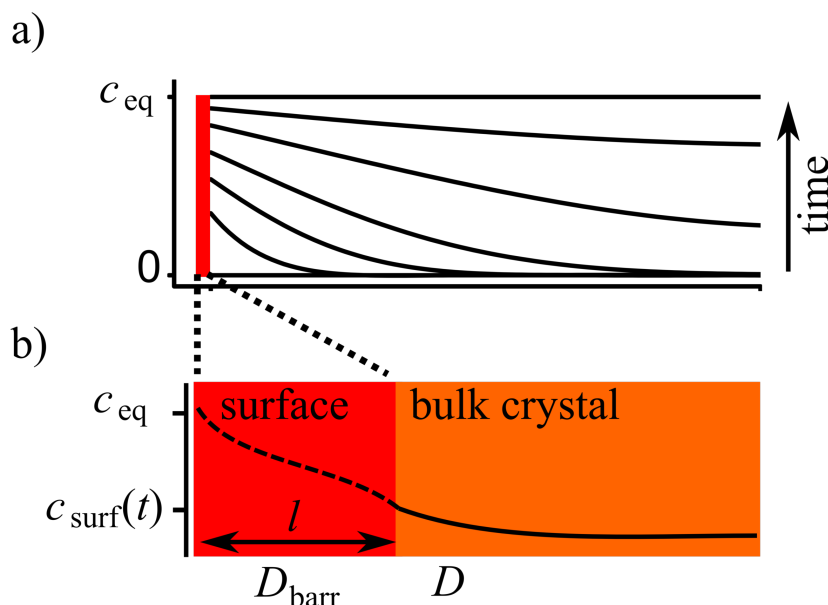


Figure 3.5: Conventional representation of a surface resistance as a thin layer of thickness l (\ll particle size L) with a dramatically reduced diffusivity D_{barr} (\ll bulk diffusivity D). The flux through the surface is driven by the difference between the equilibrium concentration c_{eq} , which is thought to be instantaneously attained on the outer side, and the concentration $c(x=0) \equiv c_{surf}$ on the inner side of the surface layer. The concentration c_{surf} is the boundary value of the evolving concentration profiles in the interior of the particle (bulk phase) as observable by IFM and IRM.

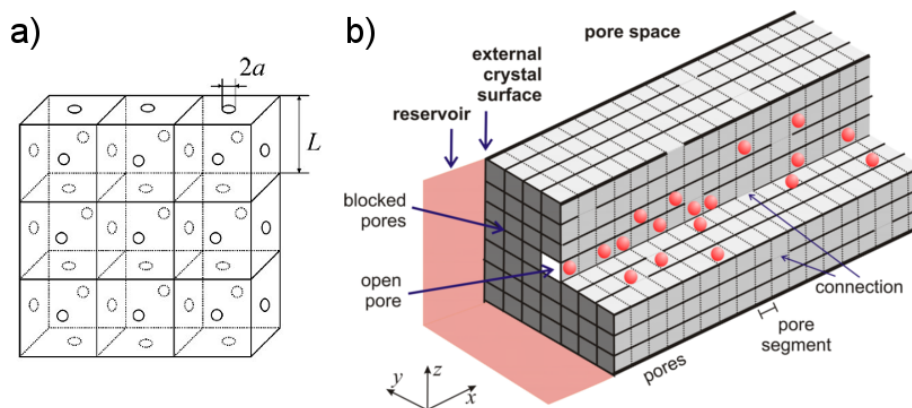


Figure 3.6: a) Geometry used by Dudko *et al.* to model diffusion and surface permeation [72]. b) Simulation model used by Heinke *et al.* to model diffusion and surface permeation in Zn(tbip) [73]. The molecules, represented by hard spheres (red balls), can move random walk-like in the one-dimensional pores in x -direction. The pores are interconnected by randomly distributed intersections that occur with an equal probability p in y - and z -direction. Transport barriers at the surface are created by blocking pore entrances at the surface [74].

In [73] Heinke demonstrates that the concentration profiles gained in his simulations resemble those measured with interference microscopy: The position in the yz -plane of the unblocked pores does not influence the shape of the concentration profiles after integration in z -direction (similar to the integration that is automatically done by the interference microscopy set-up due to the applied light transmission mode) while the position of the holes would be clearly visible in each xy - or xz -plane (Fig. 3.7b). Simulated profiles are shown in Fig. 3.7a for three different simulation times. The surface permeability derived from these profiles can be expressed according to Heinke by Eq. 3.4:

$$\alpha = 0.5 \times \frac{p_{\text{open}} D}{\lambda} \frac{5p}{1+4p} \left(1 - \frac{p}{2+4p}\right). \quad (3.4)$$

In this equation λ denotes the simulation step length which, in the Zn(tbip) structure under consideration, coincides with the separation of adjacent cages (0.82 nm, see Fig. 3.1). The amount of open pores p_{open} can easily be calculated from Eq. 3.4 in the following way:

Taking advantage of the arrangement of the cavities in one-dimensional chains (see Fig. 3.1c), the formalism of single-file diffusion allows the rates of molecular uptake and release (or of tracer exchange) to be combined to estimate the probability that molecules are able to pass each other [73]. By attributing these mutual passages to structural defects in the system, $p \approx 0.05$ is obtained. Inserting this value and $\lambda\alpha/D = 0.5 \times 10^5$ as a typical value for the mean of the dimensionless permeability/diffusivity ratios (see Fig. 3.2d), Eq. 3.4 yields $p_{\text{open}} \approx 5 \times 10^{-4}$. This result means that, on the average, within an area of about 45×45 channel entrances on the crystal surface, there is only one that is open. This estimate holds for a statistical distribution of open channel entrances. For clustered channel openings and a given surface permeability, the percentage of open channel entrances increases in proportion with the diameter of the clusters of open channels [73].

From the experimental evidence of the diffusion and permeation studies with guest molecules in Zn(tbip), the mechanism of mass transfer through the surface of nanoporous materials is found to be quite different from the conventional picture of a surface barrier as a homogeneous layer of dramatically reduced permeability. The experimental evidence is further supported by dynamic Monte Carlo simulations and a formal analytical treatment which yield estimates of the fraction of unblocked pore entrances.

The proposed resistance model may occur quite generally at any phase boundary. While in the conventional view (Fig. 3.5) the local permeation rate anywhere on the boundary is constant, the new model (Figs. 3.6b and 3.7) represents the opposite limiting case where, with the exception of a few

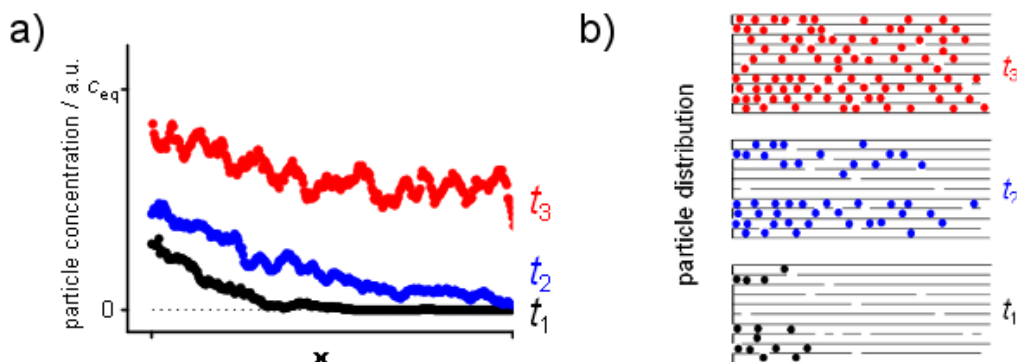


Figure 3.7: a) Concentration profiles simulated by Heinke in the geometry illustrated in Fig. 3.6. b) Possible particle distribution in the xy - or xz -plane.

unblocked entrances, all remaining pores are totally blocked.

This scenario exemplifies a situation which, in theoretical physics, is generally treated by so-called effective-medium approaches [75, 76]. In fact, for the prediction of the resulting concentration profiles it is immaterial whether one considers the real situation, i.e. a discontinuous resistance as reflected by Fig. 3.7 or a continuous surface layer (an "effective medium") with the permeability provided by Eq. 3.4 as mere inspection of the evolution of the concentration profiles in a particular experiment provides no direct evidence that would distinguish between these two models. It was the remarkable agreement between the (surface) permeabilities and (bulk) diffusivities combined with the finding of identical temperature behavior of both parameters which, for the given system, allowed the prediction of a highly discontinuous resistance with many blocked and a few open pore entrances.

In general, the nature of transport resistances may be expected to lie somewhere between the two limiting cases of a uniform low permeability (as has been widely assumed so far) and a highly heterogeneous permeability, varying between zero over most of the area and infinity for the "holes", as described here.

3.4 Aging Effects on MOF Zn(tbip) due to Storage

When sorption experiments with small hydrocarbons were performed on the metal organic framework Zn(tbip), it was observed that rate of mass transport into the crystal has dropped during several months of storage in air. Further experiments with crystals that were broken right before the experiments showed that the permeability of the surface freshly created by the

Crystal	$D(0)/$ $10^{-13} \text{ m}^2 \text{ s}^{-1}$	$\alpha_{\text{fresh}}(0)/$ 10^{-9} m s^{-1}	$\alpha_{\text{aged}}(0)/$ 10^{-9} m s^{-1}
1	2.8	7.8	1.3
2	2.1	7.6	1.5
3	3	12	2.4
4	3.8	17	4
5	2.6	12	–
mean	2.9	11.3	2.3
previous study	2.4	1.2 – 2.7	

Table 3.1: Summary of the surface permeabilities measured with propane in MOF Zn(tbip) for the aged and the freshly created surface of the crystal at zero loading as resulting from the best fits of numerical solutions of Fick’s second law to the experimental data. Crystal 5 was broken on both sides resulting in two fresh surfaces.

breakup was higher than that of the surface exposed to air during storage. This is illustrated in Fig. 3.8: The displayed concentration profiles are not symmetrical with respect to the center as the sorbat concentration increases faster on the left side of the profiles which corresponds to the freshly created surface. According to Eq. 2.15 this corresponds to an enhanced permeability of this surface. If a second fresh surface on the other end of the one-dimensional pore network is created, the profiles become symmetrical again as shown in Fig. 3.8. These findings indicate clearly that the transport reducing effect is a local one, located at the surface of the material, and not an effect that homogeneously effects the whole crystal structure. The surface permeabilities calculated for five different crystals of which four were broken on one side (crystals 1 – 4) and one crystal was broken on both sides (crystal 5) are summarized in Tab. 3.1.

In comparison with previous studies on Zn(tbip) with crystals from the same synthesis batch three months before [35, 38], surface permeabilities at zero loading are reduced by about one order of magnitude while the diffusivity is practically unchanged (Tab. 3.1)! Sample storing under ambient atmosphere is thus found to leave the intra-crystalline diffusivities essentially unaffected, while there is a dramatic enhancement of the transport resistances on the external surface of the crystals. The observed changes are in agreement with the expected behavior: structural degradation is much more likely to occur close to the crystal surface than in the crystal bulk phase. This behavior is nicely corroborated with the finding that the permeability through the fresh faces α_{fresh} of the stored crystals is of the order of the genuine surface permeabilities observed with crystals of the same batch, three months ago. After three more months under ambient atmosphere, on

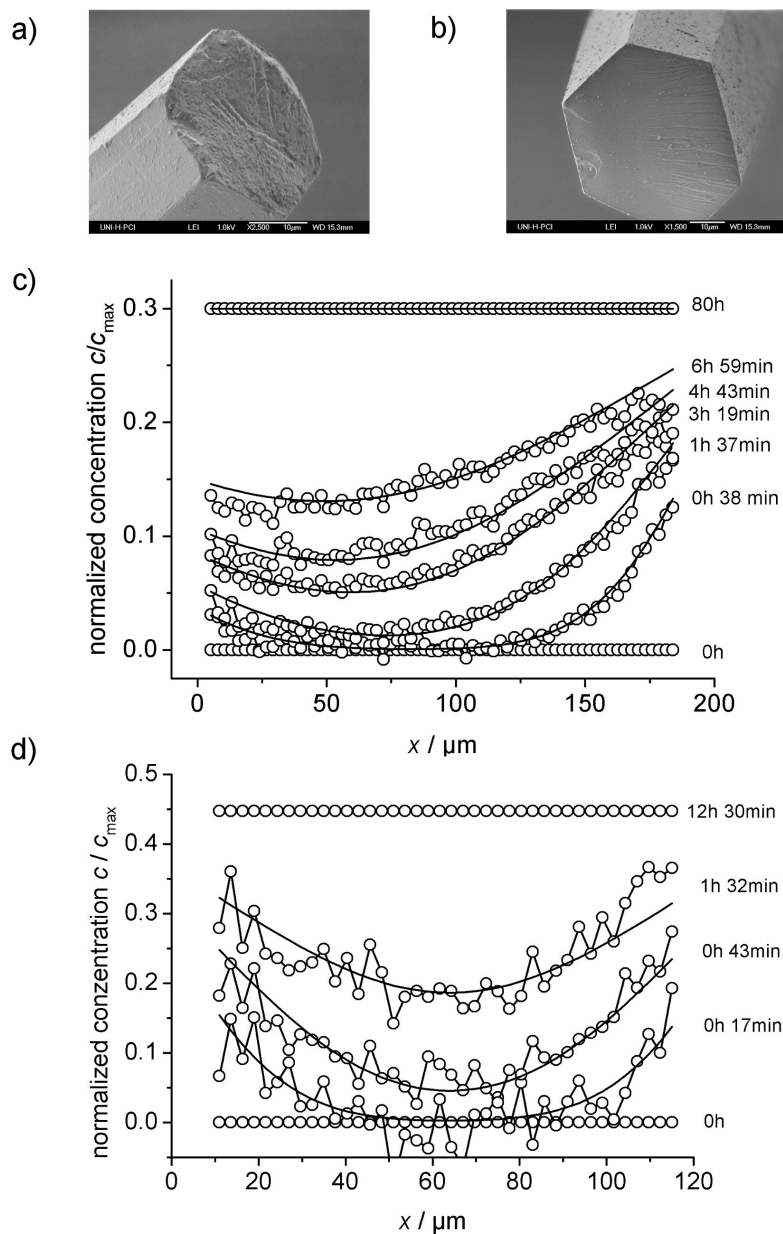


Figure 3.8: Adsorption profiles of deuterated propane in MOF Zn(tbip) crystals measured with IR-microscopy at 295 K after applying a pressure step of 0 – 30 mbar (c) and 0 – 50 mbar (d). The crystals were broken on one (c) or both (d) ends prior to the experiment in order to quantify the effects of long-time-storage on the uptake behavior. The freshly created surface (b) shows a higher rate of mass transport and therefore a higher surface permeability than the aged surface (a). Breaking the crystal on both ends results in two equally permeable surfaces. The profiles are normalized with respect to the equilibrium loading of the pressure step.

the other hand, the crystals are found to be essentially inaccessible for guest molecules.

Many MOF systems are known to be unstable in humid atmosphere. Even though the Zn(tbip) crystals are synthesized in aqueous solution and, hence, may be supposed to be stable in humid surroundings, one might speculate that, in presence of humid atmosphere, the surface is gradually oxidized leading to a formation of ZnO deposits. An aging mechanism based on moisture can also explain the variations in the observed surface permeabilities. The hydrophobicity of the channel network implicates the formation of an outer "aging front" instead of an entirely corrupted pore network. With on-going time, the front of the assumed reactions would slowly proceed towards the center of the crystal, whereas the channel interior between the fronts remains nearly unaffected. Following this model one would expect that the surface permeability decreases with aging time while the diffusivity of guest molecules doesn't change (as observed in the experiments). In this context one can also rationalize that the surface permeability of the broken faces was in the same order as the permeabilities of the untreated faces of the first experiments, rather than notably exceeding them. While breaking the crystal, it was tried to break away only a small part of the material. It might be possible, therefore, that such an "aging front" has got already to the position of the freshly broken face. Alternatively, one could clearly argue that the breaking process itself creates structural defects on the surface which result in a reduced surface permeability.

Further evidence that the observed effect is a surface effect is given by SEM pictures taken from freshly created and aged crystal surfaces: While the freshly created surface looks sound and plain, the aged surface is covered by a rough layer which is supposed to be blocking a certain amount of the pore entrances (Fig. 3.8a and b).

The effect of the differences in the permeabilities on overall mass transport may be illustrated by considering the total fluxes entering the crystal through the different faces. Following [77], the relative amount of molecules $N_{\text{fresh}}^{\text{rel}}$ entering the crystal through the freshly broken face may be noted to be

$$N_{\text{fresh}}^{\text{rel}} = \frac{\tau_{\text{fresh}}^{-1}}{\tau_{\text{fresh}}^{-1} + \tau_{\text{old}}^{-1}} \quad (3.5)$$

with

$$\tau_{\text{fresh/old}} = \frac{l}{\alpha_{\text{fresh/old}}} + \frac{l^2}{3 \cdot \bar{D}} \quad (3.6)$$

where l denotes the half length of the crystal channels and $\bar{\alpha}$ and \bar{D} denote

the mean values of the permeability and diffusivity over the considered concentration interval. Since the concentration dependencies of the diffusivities and permeabilities were found to coincide, the evaluation of Eqs. 3.5 and 3.6 may be simply based on the permeabilities and diffusivities for zero loading. For the crystals under investigation, with half lengths of about 100 μm and $\alpha_{\text{fresh}}(0)/\alpha_{\text{old}}(0) \approx 5$, almost 75% of the total amount of molecules are found to enter the crystal through the fresh surface. This value will even increase for shorter crystals or higher intra-crystalline diffusivities, making gradually increasing surface barrier during the usage of porous materials responsible for severe reduction of the performance of the material: The formation of surface barriers during crystal production, storage or technological use is an unintentional, but often inevitable, effect that may lead to a serious aggravation of the crystal performance. The presented experimental results and their evaluation might contribute to a better understanding of the consequences of the storage conditions for the crystal performance.

Considering the fundamental importance of surface barriers for many industrial applications, the detailed exploration of the mechanisms of their generation is an important and most attractive task for further investigations, including the option of their exploitation for the tailoring of crystal properties for specific applications.

Chapter 4

Diffusion in FER Type Zeolite

4.1 Motivation

Zeolite crystals of the FER framework type [52] have been in the focus of IFM and IRM experiments for several years due to the high reproducibility and reliability of the experimental results and their experimentally advantageous pore structure (see section 2) [78–80].

Ferrierite crystals provide particularly favorable properties for diffusion studies by interference and IR-microscopy. The pore space of ferrierite consists of two, mutually intersecting, sets of parallel channels, which are formed by rings of 10 oxygens and silicons ($0.42 \text{ nm} \times 0.54 \text{ nm}$, called *10-ring channels*, [001]-direction, longitudinal axis of the crystal, Fig. 4.1c) and 8 oxygens and silicons ($0.35 \text{ nm} \times 0.48 \text{ nm}$, called *8-ring channels*, [010]-direction, Fig. 4.1b), respectively (Fig. 4.1a, [52]). The pore system might be visualized - over emphasized - as a road map of chess board-like structure with broad and straight highway in one direction and narrow and curved streets perpendicular to them (Fig. 4.1a). Comparable to traffic in such a road system, anisotropic behavior of the molecule transport would be expected, with fast transport in the larger 10-channels and slower transport due to sterical hindrances in the 8-ring channels. This pore network makes zeolites of type ferrierite particularly convenient for micro-imaging experiments as all complications in profile analysis caused by molecular fluxes in observation direction [81] can be avoided by choosing the direction of observation perpendicular to the plane of the pore network.

However, in former experiments with methanol the experimentally observed transport behavior was found to deviate strongly from the expected one. The main reason for that observation was a strong transport barrier located on the entrances of the 10-ring channels that lead to a dramatic reduction of the material uptake along the 10-ring channels and therefore to a dramatic deceleration of the overall sorption process [30, 71, 79].

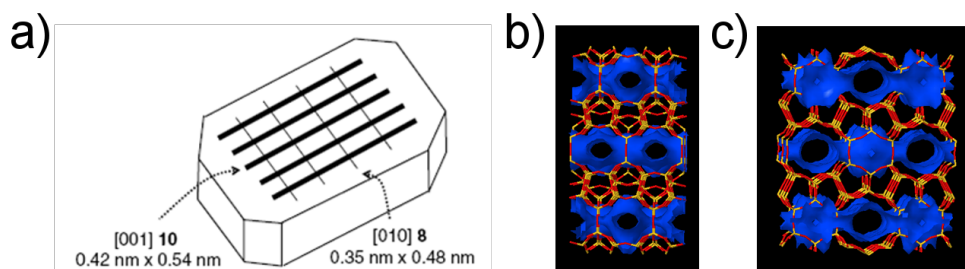


Figure 4.1: a) Illustration of the pore network in ferrierite type crystals. The two-dimensional network consists of interconnected 8- and 10-ring channels. In IFM and IRM experiments the pore network is typically oriented perpendicular to the observation direction. b) Pore space viewed in 8-ring channel direction. c) Pore space viewed in 10-ring channel direction.

Ferrierite can be synthesized in the shape of thin platelets and elongated hexagons with the channel system extended in the largest plane of the crystallites. The chemical composition depends on synthesis. The silicon to aluminum ratio can be changed from infinity (pure silicon form) to 10. Aluminum can also be replaced by boron. In that case silicon to boron ratios around 300 have been reported [82].

For the experiments I will present in the next sections, I used two different ferrierite samples of the all silica type of this material. The first sample is identical with the sample used by Kortunov *et al.* [78, 79] in his experiments with methanol [83]. Kortunov's experiments were restricted to room temperature due to the restrictions of the experimental set-up at that time. The experiments I will present were done at elevated temperatures after a fundamental update (see section 2.1) of the experimental set-up that now allows experiments at temperatures up to 100°C. These experiments might be seen as bridge, connecting the work of my predecessor with the work of my own .

The second sample I used in my experiments was produced by Marthala *et al.* in the course of a joined research project [82]. The experiments on these materials were motivated twofold. First, it should be tested if ferrierite crystals could be advantageous candidates as catalysts for the in-situ observation of transient concentration profiles during chemical reactions, benefiting from their pore structure which is particularly suitable for micro-imaging and - as assumed prior to the experiments - for fast transport of the molecules participating in the reactions. In this context the uptake of different small hydrocarbons was studied and compared. Second, the materials should be tested for the transport resistance formerly observed on the first sample and a method to remove these resistances should be found in collaboration with

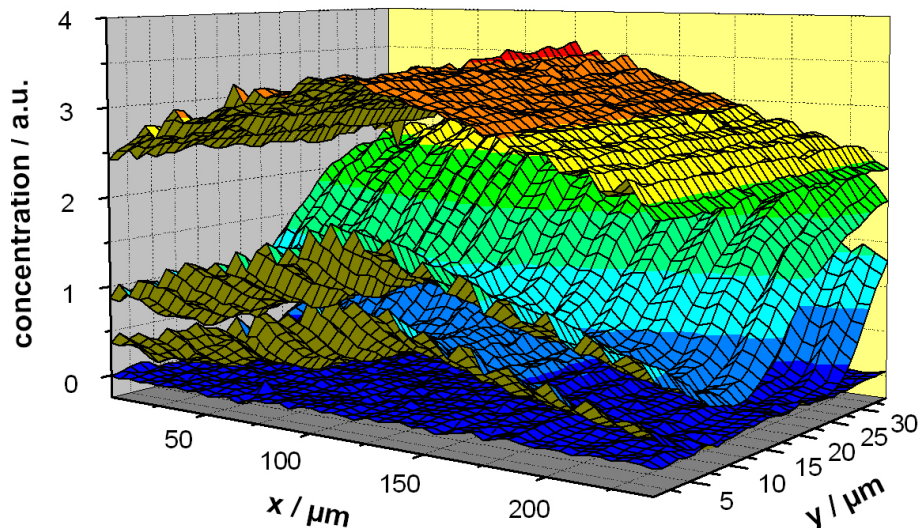


Figure 4.2: Evolution of the apparent methanol concentration (c_{app} , see section 2.1) as measured during an uptake experiment initialized by the pressure step 0 – 130 mbar in the surrounding methanol pressure at 323 K.

our co-workers in the project.

4.2 Diffusion of Methanol in Ferrierite

4.2.1 Diffusion in 8-Ring Channels at Elevated Temperatures

For these experiments large ($30 \mu\text{m} \times 200 \mu\text{m} \times 10 \mu\text{m}$) all-silica single crystals of FER which have been synthesized as described in [83] were used. In this synthesis, the entrances to the 10-ring channels on the outer surface are almost blocked [30, 71], so that uptake is dominated by diffusion along the 8-ring channels. Therefore, and owing to the uniform thickness of the crystals in the direction of the 8-ring-channel, IFM is able to directly provide the profiles of intra-crystalline concentration along the 8-ring channels. These profiles, the starting point for the exploration of the different mechanisms contributing to overall mass transfer, are shown in Figs. 4.2 and 4.3.

Prior to the experiments, the crystals have been calcined and activated at $450 \text{ }^\circ\text{C}$ for at least 10 hours under vacuum. Experiments were started by an essentially instantaneous increase of the pressure in the surrounding

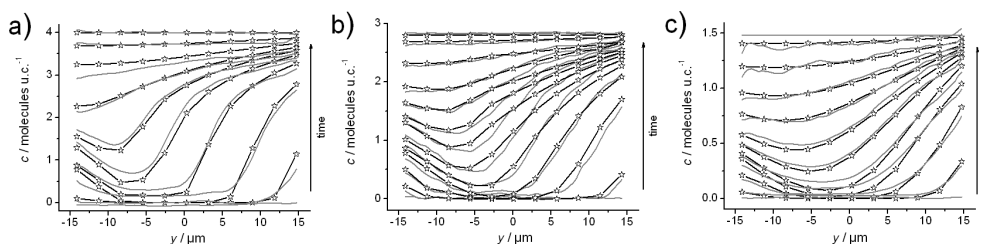


Figure 4.3: Transient concentration profiles of methanol in all-silica FER along the direction of the 8-ring windows (y -direction in Fig. 4.2) at $x = 220 \mu\text{m}$ induced by a pressure step in the surrounding (methanol) atmosphere from zero to 120 mbar at 295 K (a), to 130 mbar at 323 K (b) and to 145 mbar at 353 K (c). The asymmetric shape of the profiles is caused by different permeabilities of the surfaces. *Broken* line: experimental data, *full* line: simulation results. For calculated diffusivities and surface permeabilities see Tab. 4.1.

atmosphere from zero to a constant, final value. Measurements have been performed at room temperature (the only temperature considered in previous studies [30, 71]) in order to provide comparability to the previous experiments and at elevated temperatures of 323 K and 353 K. In the latter case, before and during the experiment, the whole experimental set-up (Fig. 2.1), the guest molecules and crystals were kept at identical and constant elevated temperatures, ensured by an appropriate heating of both the external reservoir of the guest molecules and the optical cell with the crystals [39, 40].

Due to the underlying measurement principle, IFM provides quantitative information about only relative rather than absolute changes in concentration. This deficiency was compensated by combination with the information of adsorption isotherms for the relevant temperatures and pressures, stemming either from real experiments or theoretical estimates. In the present case, either option is used by exploiting the results of IR microscopy measurements with the system under study [79, 84] and of Configurational-Bias Monte Carlo (CBMC) simulations [85, 86].

Figure 4.4b shows the adsorption isotherms of methanol in all-silica FER as resulting from CBMC simulations. The experimental data obtained by IR microscopy at room temperature are adjusted to the theoretical predictions. Also indicated are the concentrations which, after equilibration at the final pressure, result from the IFM measurements for the different temperatures considered. They were calibrated on the basis of the IR data for room temperature.

Figure 4.3 provides an overview of the transient profiles of guest concentration along the direction of the 8-ring channels (y -direction) recorded by IFM during molecular uptake induced by the application of a guest pressure

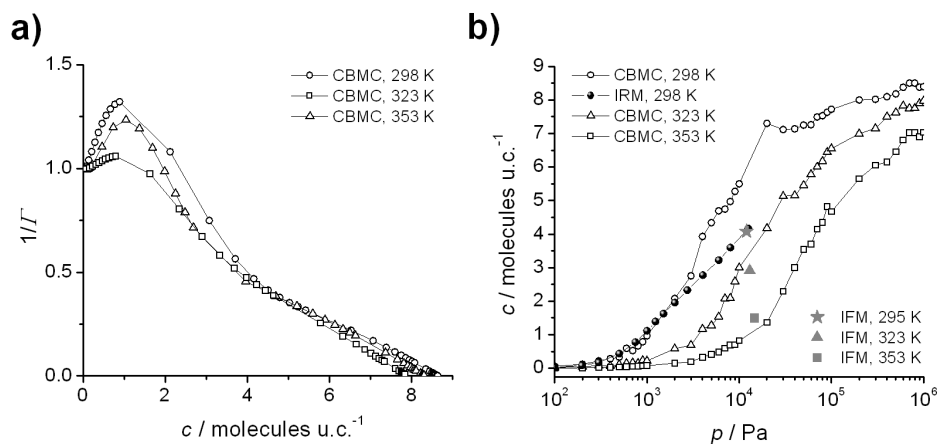


Figure 4.4: Equilibrium data for methanol adsorption on all-silica FER (one unit cell (u.c.) comprises two 10-ring channel segments and two cavities of 6-7 Å diameter, enclosed by 6- and 8-ring windows [52]). a) Inverse thermodynamic factor $\Gamma^{-1} = \partial \ln c / \partial \ln p$ calculated from the simulated adsorption isotherms. b) Adsorption isotherms determined by CBMC simulation and comparison with the experimental results obtained by IR microscopy and IFM.

in the surrounding atmosphere at different temperatures. The guest concentrations are indicated on the basis of the calibration provided by Fig. 4.4b.

Immediately visible, one notes the asymmetry in the concentration profiles caused by permeabilities of the two surfaces. In contrast to the experiments presented in section 3.4 in which the crystals were modified intentionally in order to create surfaces of different permeability, here this observation was surprising and completely unintentional and not supported by modifications of the crystal. It was proved by experiments of the last years that identically structured surfaces of a single crystal tend to have very similar permeabilities while there might be small deviations between different crystals of the same batch. It is therefore unlikely that the observed diverging permeabilities were created during the synthesis or during storage. The present observation might be explained indeed by cracks in the surface with the higher permeability. In chapter 5 the influence of cracks on mass transport is briefly discussed and it is shown that cracks might enhance the rate of mass transport through a surface. In the two-dimensional FER structure this effect might even be amplified due to the higher diffusivity in the 10-ring channels that leads to a fast molecule distribution in the 10-ring channel which might be interpreted as a homogeneous increased surface permeability.

Another anomaly becomes evident with the presentations in Fig. 4.5a. It provides the data which, with the system under study and under the chosen experimental conditions, would result in conventional diffusion mea-

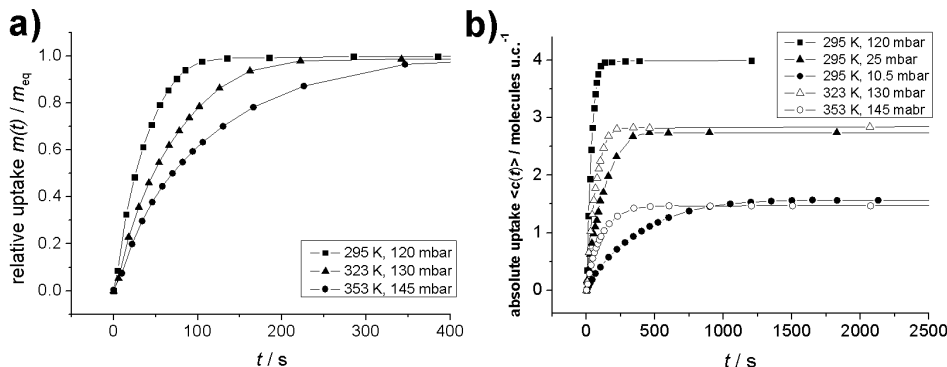


Figure 4.5: Time dependence of methanol uptake $m(t)$ along the 8-ring channels of all-silica FER as resulting from Fig. 4.2 by employing Eq. 2.3, represented (a) as the relative uptake $m(t)/m_{\text{eq}}$ (with $m_{\text{eq}} = m(t \rightarrow \infty)$) and (b) as the absolute uptake, in terms of the mean concentration $\langle c(t) \rangle = \int_{-l_y}^{l_y} c(t, y) dy / (2l_y)$. Also included in (b) are the results of complementary experiments at room temperature with smaller pressure steps, chosen in such a way that the resulting equilibrium concentrations m_{eq} are those of the experiments at elevated temperatures.

surements, considering only the relative molecular uptake: It appears that, under the chosen experimental conditions, the rate of overall molecular uptake decreases rather than increases with rising temperature.

By implying an ideal, homogeneous crystal bulk phase, the evolution of the intra-crystalline concentration follows Fick's 2nd law (Eq. 2.10) with the initial condition $c(y, t = 0) = 0$ and a surface barrier as defined in Eq. 2.15 as boundary condition at $y = \pm l_y$.

The coefficient of intra-crystalline transport diffusion D (generally referred to as the transport diffusivity) is, in general, a function of both temperature and concentration and is assumed to be uniform within the crystal. The surface permeability on either side of the crystal ($y = \pm l_y$), which is also a function of temperature and loading, is denoted by α_{\pm} . Since the concentration range relevant for surface permeation covers a whole interval, namely from $c(y = \pm l_y)$ to c_{eq} , it cannot as easily as the transport diffusivity be attributed to one concentration, namely the given, local one. However, by considering a large variety of intervals $c(y = \pm l_y)$ to c_{eq} , it was found in [35] that the concentration dependence of the surface permeabilities can be satisfactorily taken account of by considering their dependence on the mean concentration $(c(y = \pm l_y) + c_{\text{eq}})/2$. The surface permeabilities are assumed to be uniform on either side of the crystal while, in view of the asymmetry in the concentration profiles, they are clearly anticipated to be vastly different on the two crystal sides.

T/K	Surface Permeability		Transport Diffusivity	
	$k_0/$ 10^{-8} m s^{-1}	$k_1/$ $(\text{molec./u.c.})^{-1}$	$k_0/$ $10^{-13} \text{ m}^2 \text{ s}^{-1}$	$k_1/$ $(\text{molec./u.c.})^{-1}$
295	6.5	1.1	2	1.5
323	8.9	1.2	3.4	1.4
353	12.3	1.5	7.2	1.3

Table 4.1: Fitting parameters used for the analytic representation of the concentration dependence of the intra-crystalline transport diffusivities (D) and of the surface permeabilities (α_+) through the crystal boundary at $y = +l_y$ (right-hand side in the representations of Fig. 4.3). Both quantities could be approached by relations of the form $k_0 \cdot \exp(k_1 c)$ with the parameters k_0 and k_1 as given in the table.

The surface permeabilities are calculated via Eq. 2.15, realizing that the fluxes $j(y = \pm l_y)$, i.e. the number of molecules passing the crystal surface per area and time, may be calculated by considering the area between the concentration profiles determined at two subsequent instants of time, taken from the crystal boundary to the profile minima, divided by the time interval between these two measurements. In this way, the surface permeabilities through the crystal boundary at $y = +l_y$ were found to be reasonably well approached by assuming an exponential dependence of the form $k_0 \cdot \exp(k_1 c)$. The values of the fitting parameters k_0 and k_1 as determined for the different temperatures are summarized in Tab. 4.1.

It was impossible to determine the surface permeability through the crystal boundary at $y = -l_y$ with a similar accuracy, as the reduced permeability leads to a notably smaller flux into the crystal which results in a slower concentration increase and, hence, in a shift of the concentration minima towards $y = -l_y$. The area between subsequent concentration profiles and between the crystal boundary and the location of the concentration minimum on this side of the crystal could, therefore, be determined with only a very high uncertainty which accordingly leads to equal uncertainties of the surface permeabilities. However, due to the same reason, namely the notably reduced guest flow into the crystal, the surface permeabilities on this side of the crystal are also of minor relevance for the evolution of the concentration profiles [87]. Without significant influence on the resulting concentration, the surface permeabilities on this side of the crystal can therefore be assumed to be independent of concentration. This constant value was implied to be equal to the mean value estimated, for each time interval between subsequent concentration profiles for the surface permeability. The thus determined values ($\alpha_- = 5.5, 5.9$ and $5 \times 10^{-8} \text{ m}^{-1} \text{ s}^{-1}$ for 295, 323 and 353 K, respectively) don't vary notably with the temperature either.

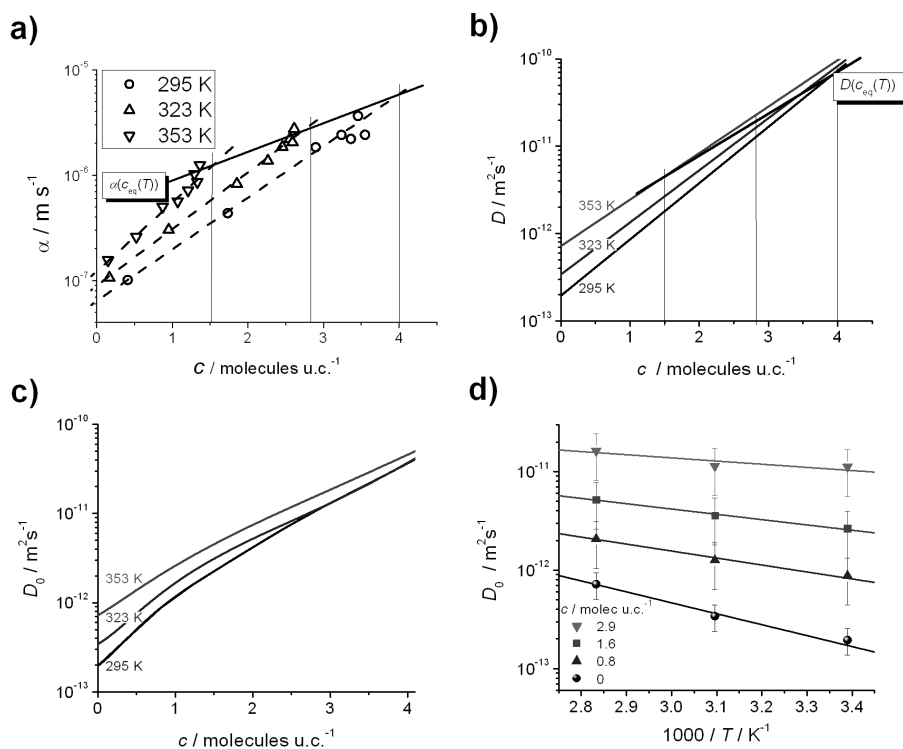


Figure 4.6: Surface permeability on the more permeable side (a) and intra-crystalline transport diffusivity (b) of methanol in the direction of the 8-ring channels of an all-silica crystal of type FER in dependence on the methanol concentration for the three temperatures considered in the experiments, determined with the parameters of Tab. 4.1. By connecting the data points to be expected for the final loadings, both the surface permeabilities and diffusivities are seen to be the smaller the larger the temperatures are. Figures 4.6c and d show the corrected diffusivities calculated via Eq. 2.13 with the thermodynamic factors of Fig. 4.4a as a function of both loading (c) and temperature (d).

With these assumptions about the surface permeabilities and the thus specified boundary conditions, the measured concentration profiles were fitted using the finite-difference solution introduced in section 2.4.2. It appeared that, as already with the surface permeability on the crystal side of higher permeability, the observed profiles may be satisfactorily reproduced by assuming an exponential approach for the concentration dependencies of the diffusivities. The relevant data are summarized in Tab. 4.1 and the concentration profiles resulting from the simulations are shown by the full lines in Fig. 4.3. The asymmetry observed in the concentration profiles indicates, in the same way as discussed in section 3.4, a pronounced difference in the surface permeabilities on the two crystal faces in the entrance planes of the 8-ring channels.

The deceleration of molecular uptake with increasing temperature as observed via the uptake curves plotted in Fig. 4.5a, is illustrated in Figs. 4.6a and b by the displayed surface permeabilities and intra-crystalline diffusivities. As to be expected, for concentrations kept fixed, both the surface permeabilities and intra-crystalline diffusivities clearly increase with increasing temperature. In the experiments documented in Figs. 4.3 and 4.5a, however, temperature increase is seen to be accompanied by a decrease in loading. The representations of Figs. 4.6a and b show that the decrease in the surface permeabilities caused by this decrease in the loadings (caused by the temperature increase) overcompensates the diffusion accelerating effect of temperature increase, resulting in an overall decrease in both the surface permeabilities and diffusivities, i.e. in a deceleration of uptake with increasing temperature as appearing from Fig. 4.5a. This argumentation is supported by Fig. 4.5b in which the time dependence of molecular uptake in absolute rather than relative units is shown. In addition to the data, re-plotted from Fig. 4.5a, they do also include the results of uptake measurements at room temperature with notably reduced pressure steps chosen in such a way, that the final loadings did coincide with those attained with the larger pressure steps at higher temperatures. Now, in complete agreement with the expectation, uptake rates are seen to increase with increasing temperature.

Opposite to the mechanisms giving rise to the formation of transport resistances on the surface of nanoporous materials (see section 2.3.2), the transport diffusivities are well known to be affected by two influences, which become particularly evident by using the Maxwell-Stefan notation (Eq. 2.13, also referred to as the Darken equation). The corrected diffusivity D_0 is a measure of the translational mobility of the guest molecules and coincides with the self-diffusivity if the guest-wall interaction notably exceeds the influence of the guest-guest interaction on the molecular propagation rates (section 2.3.2). Figure 4.4b shows the reciprocal values of the thermodynamic factor Γ , which is required for the calculation of D_0 from the transport diffusivities, determined from the adsorption isotherms of Fig. 4.4a. With this representation, the decrease in loading from about 4 molecules per unit cell at 295 K to about 2.5 at 323 K and 1.5 at 353 K is seen to be accompanied by a significant increase of the thermodynamic factor and hence, with Eq. 2.13 (Darken equation), by the increase of one of the factors constituting the transport diffusivities.

Figure 4.6c shows the concentration dependence of the corrected diffusivity as resulting from Eq. 2.13 with the thermodynamic factors given in Fig. 4.5b. Also here, by simultaneously increasing the temperature and decreasing the loading, the resulting corrected diffusivities are found to decrease with increasing temperature, as a consequence of the dominating influence

of the loading dependence.

In contrast to the thermodynamic factor which for Langmuir-type isotherms is well known to increase with increasing loading, the observed increase in the corrected diffusivities with increasing loadings is only one pattern among a multitude of concentration dependences observed for the intra-crystalline mobilities. The present dependencies (referred to as the type-V concentration pattern [88, 89]) may result if the activation energy for molecular propagation decreases with increasing loading [90, 91]. Such a model is in complete agreement with the Arrhenius presentation of the corrected diffusivities in Fig. 4.6d, where the activation energies (slopes in the representations) decrease with increasing loading, in parallel with a significant increase in the absolute values of the diffusivities.

With the experiments presented here the reasons for two remarkable findings could be cleared by attributing the experimental results to their microscopic/microdynamic origin, namely (i) a pronounced asymmetry in the concentration profiles which is ascribed to notably different guest permeabilities on either side of the crystals and (ii) a slowing down of molecular uptake with increasing temperature for essentially identical pressure steps, which can be related to a dramatic concentration dependence in both the surface permeability and intra-crystalline diffusivities.

4.2.2 Diffusion Anisotropy

Mass transport in ferrierite was also studied most thoroughly with methanol in new all-silica ferrierite material produced according to the synthesis published in [82] by Marthala *et al.*. First experiments on the as-synthesized material resulted in observations similar to those obtained with the old sample discussed in the previous section: Uptake could be observed via the 8-ring channels of the materials but not (or at least again strongly retarded) along the 10-ring channels. Figure 4.7 shows some of the concentration profiles detected with IRM during an adsorption experiment with methanol. It is evident from the profiles that the concentration increases from the *right* and *left* edge of the crystal which corresponds to the direction of the 8-ring channels and not from the bottom where the entrances of the 10-ring channels are located. After numerous tests with different acids and bases and the application of ultrasonics, a mild NaOH treatment was found to remove (or at least notably reduce) the blockage at the entrances of the 10-ring channels while the crystal structure was not influenced [82].

Figure 4.8a shows a collection of concentration profiles measured during the uptake of methanol after the NaOH had been applied. Although the

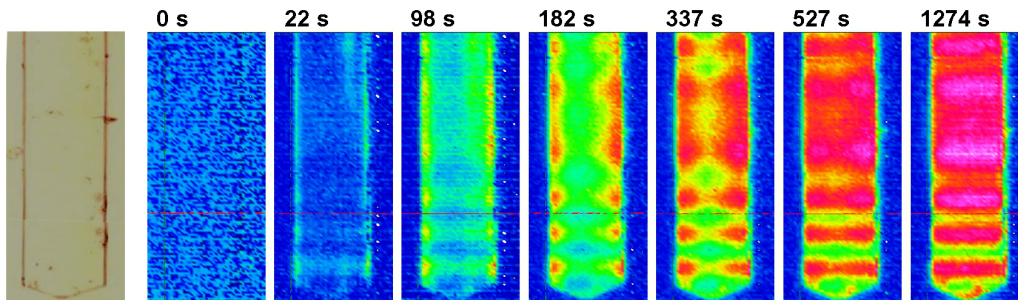


Figure 4.7: Picture of the all-silica ferrierite crystal (*left*) and concentration profiles of methanol as measured with IRM in imaging mode during adsorption from 0 mbar to 10 mbar at room temperature. The uptake occurs in horizontal (8-ring channel) direction and not via both channel types. Concentration increases from *blue* to *green* to *yellow* to *red*.

crystal in which the profiles shown in Fig. 4.8a and Fig. 4.7 were measured came from the same synthesis batch and differ only in post-synthesis treatment (no treatment vs. NaOH etched), the difference in the uptake pattern is quite obvious: After NaOH treatment the uptake occurs from all four crystal surfaces which should also theoretically be accessible for mass transport and therefore via 8- and 10-ring channels.

A close inspection and comparison of the measured profiles reveals the following features:

(i) Transient concentration profiles in horizontal (10-ring channel) direction at the crystal boundaries assume the equilibrium concentration after time intervals which are very short in comparison with the propagation of the diffusion front into the crystal interior. The influence of transport resistances at the crystal surface (surface barriers) is found to be negligibly small in comparison with the diffusion resistance of the zeolite pore network due to the post-synthesis treatment with NaOH solution [82].

(ii) The rate of mass transfer in ferrierite is seen to be highly anisotropic: in complete agreement with previous expectations, the propagation speed of the diffusion front in x -direction (i.e. along the 10-ring channels, Fig. 4.8b) is notably faster than in y -direction (along the 8-ring channels, Fig. 4.8c).

(iii) There is a decisive difference in the shape of the concentration profiles along the 10- and 8-ring channels (Figs. 4.8b and c). Up to medium observation times, the evolution of the concentration profiles in Fig. 4.8b is intuitively seen to follow the pattern of diffusion-controlled uptake where, via Fick's 2nd law (Eq. 2.10) an increase in concentration is easily seen to be caused by a curved concentration profile (non-vanishing second derivative) and, for diffusivities D depending on concentration, by non-vanishing

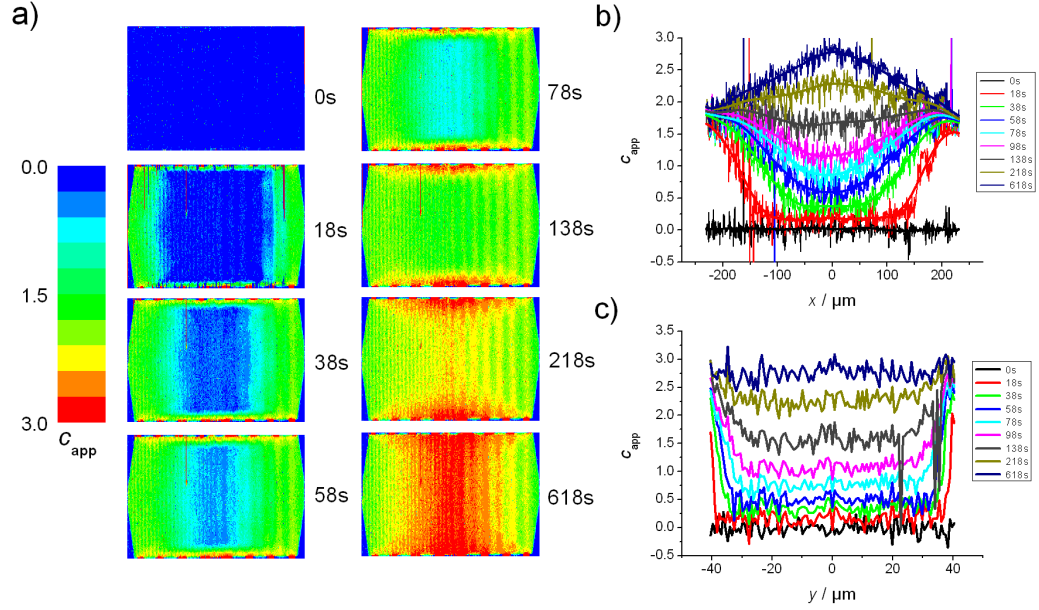


Figure 4.8: Evolution of guest concentration during adsorption following a pressure step from 0 - 5 mbar methanol in two-dimensional profiles (a) and along the x - and y -axis of the crystal (b),(c). The one-dimensional profiles are taken from the middle of the crystal at $x = 0$ or $y = 0$.

first derivatives. In contrast to Fig. 4.8b, both these implications would not hold for the central part of the profiles shown in Fig. 4.8c. Obviously, guest concentration in these parts of the crystal increases by diffusion fluxes along the 10-ring channels, rather than the 8-ring channels, i.e. by fluxes in the direction perpendicular to the profiles shown in Fig. 4.8c.

(iv) Eventually, with further increasing observation times, the imaging profiles in Fig. 4.8b are seen to pass a maximum in the crystal center. This maximum occurs in consequence of the particular shape of the crystals (Fig. 4.9a) with Eq. 2.2 the primary data c_{app} of the imaging experiment are easily seen to become eventually – i.e. after attaining a uniform local concentration $c(x, y, z) = c_{eq}$ all over the crystal – directly proportional to the crystal thickness $L(x, y)$. Since the crystals (platelets, see Fig. 4.9a) are thickest in their center, it is also in this center where the experimentally determined values of c_{app} have to attain their maximum.

(v) It is worthwhile noting that, in addition to uptake in x -direction by the main crystal body, uptake by the roof-like parts of the crystals leads to a further, uniform increase in (apparent) concentration which is easily recognized by an base-line shift after the first time steps in Figs. 4.8b and c.

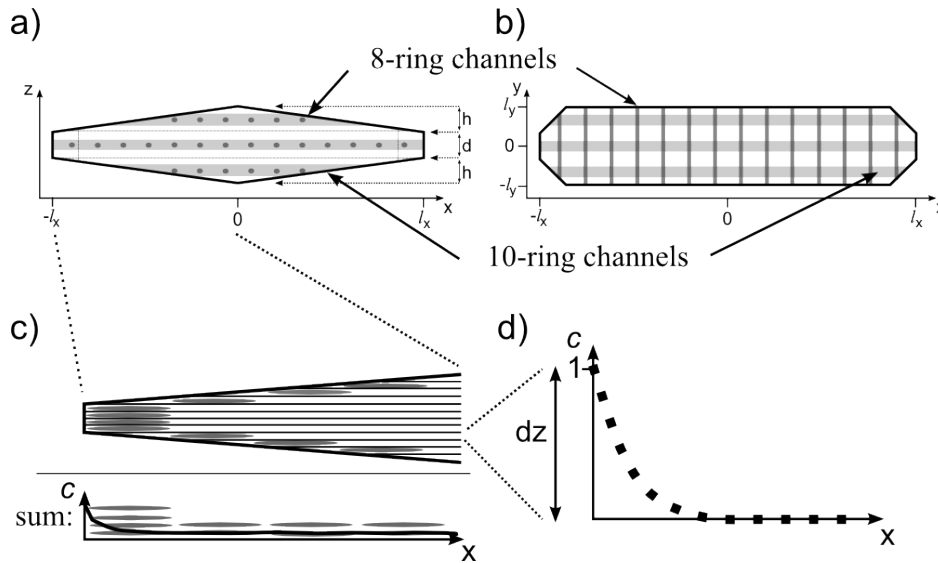


Figure 4.9: Side view (a) and top view (b, as seen through the microscope) of a typical ferrierite crystal used in this work. In an experiment the crystal lies in the xy -plane, assigning the z -direction as observation direction. Interconnected 10- and 8-ring pores run in x - and y -direction, respectively. For further analysis the crystal is divided into thin slices of thickness dz . Profiles $c(x, t)$ (d) are identical in all slices, starting with the equilibrium concentration at the crystal surface.

Application of the Boltzmann-Matano Method for Data Analysis

The shape of the studied crystals is illustrated in Fig. 4.9. The crystals appear as platelets with half-lengths l_x and half-widths l_y of typically hundreds and tens of micrometers and a (mean) thickness $d + h$ of about 10 μm wherein d denotes the thickness of the main body of the crystal and h denotes the maximum height of the roof-like part, attached in observation direction to the main body as indicated in Fig. 4.9a.

Computer algorithms applied so far for profile analysis were not able to take the shape of a crystal and its influence on the measured profiles into account. Therefore it was necessary to find a way to calculate the real concentration $c(x, y, z)$ from the measured apparent concentration in order to use the established routines for data analysis. A mere normalization of the measured concentration profiles by dividing each profile by the equilibrium profile is not sufficient as short (10-ring) channels in the roof-like parts are filled faster than the channels in the main body.

According to Eq. 2.2, the local concentration $c(x, y, z)$ appears as the kernel of an integral, which can be determined by transferring Eq. 2.2 into a corresponding differential equation. Fig. 4.9c visualizes that the totally recorded apparent concentration $c_{\text{app}}(x, y)$ is the superposition of the con-

centrations attained at this instant of time in each individual layer at the given position (x). The required mathematical treatment can be simplified notably by assuming sufficiently short time spans so that the total amount of guest molecules which, at time t , have got to the crystal center ($x = 0$) is negligibly small. In this case, the concentration profiles can be assumed to be identical in all layers, with the only distinction that, in the roof-like parts of height h below and on top of the crystal main body, the profiles are shifted towards the crystal center. Since guest propagation in y -direction is by orders of magnitude slower than in x -direction, by considering the concentration profiles in x -direction in the very center of the crystal ($y = 0$) any contribution by guest fluxes in y -direction may be neglected.

With this assumptions, the apparent (measured) concentration can be described by the relation

$$c_{\text{app}}(x) = d \cdot c(x) + \frac{2h}{l_x} \int_0^x c(\xi) d\xi \quad (4.1)$$

from which one obtains

$$\frac{dc_{\text{app}}(x)}{dx} = d \cdot \frac{dc(x)}{dx} + \frac{2h}{l_x} c(x) \quad (4.2)$$

with the normalized solution [92]

$$c(x) = \exp\left(-\frac{2h}{d \cdot l_x} x\right) \times \left(1 + \frac{1}{d} (c_{\text{app}}(x) \cdot \exp\left(\frac{2h}{d \cdot l_x} x\right) - c_{\text{app}}(0)) - I(x)\right) \quad (4.3)$$

where the following notation was used

$$I(x) = \frac{2h}{d^2 \cdot l_x} \int_0^x c_{\text{app}}(\xi) \cdot \exp\left(\frac{2h \cdot \xi}{d \cdot l_x}\right) d\xi . \quad (4.4)$$

Figure 4.10a shows the smoothed profiles of the apparent concentration $c_{\text{app}}(x)$ taken at $y = 0$ which were inserted into Eqs. 4.3 and 4.4 for determining the "true" (local) concentration $c(x)$. The resulting concentration profiles $c(x)$ in the main crystal body (of thickness d) are shown in Fig. 4.10b. They reappear, correspondingly shifted in x -direction, in the roof-like parts of the crystal.

By modifying Fick's 2nd law (Eq. 2.10), the concentration profiles during diffusion-limited uptake into an infinitely extended medium can be shown to merge to a master curve if plotted as a function of x/\sqrt{t} rather than x (Fig. 4.10c). Plots of this type are the starting point of the application of the Boltzmann-Matano method discussed in section 2.4. Fig. 4.10c shows the correspondingly transferred concentration profiles of Fig. 4.10b. The

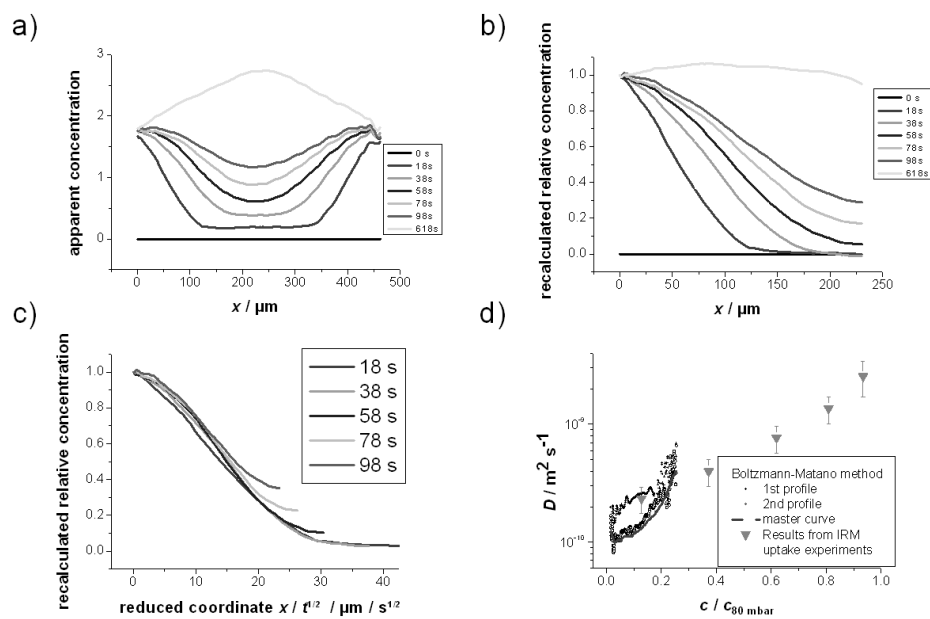


Figure 4.10: (a) Evolution of the apparent guest concentration (smoothed) along the 10-ring channels during adsorption by a pressure step from 0 to 5 mbar methanol in the surrounding atmosphere. These profiles are used for the recalculation of the actual concentration profiles $c(x)$ (b) in x -direction which merge to a master curve if plotted as a function of x/\sqrt{t} rather than x (c). The concentration dependence of the diffusivities determined via Eq. 2.18 follows the trend predicted by the diffusivities estimated from IRM uptake measurements (d).

reasonable agreement up to diffusion times of about 40 s illustrates that the implications inherent to the Boltzmann-Matano method are fulfilled. Obviously, with further increasing time, the amount of molecules which have got into the crystal center ($x = 0$ in Figs. 4.9a and 4.8b, corresponding to $x \mu\text{m}$ in Figs. 4.10c and b) cannot be considered to be negligibly small anymore. Hence, the crystal extension cannot be considered to be infinitely large and the implication for the application of the Boltzmann-Matano transformation are no more fulfilled.

Figure 4.10d shows the concentration dependence of the diffusivity of methanol along the 10-ring channels in all-silica ferrierite as resulting via Eq. 2.18 from the transient concentration profiles (Figs. 4.10a to c) recorded 18 s and 38 s after the onset of adsorption. The two data sets illustrate the uncertainty in the diffusivities if referred to a single profile. The broken line in Fig. 4.10d results by applying Eq. 2.18 to the mean of the master plots shown in Fig. 4.10c. Further shown in Fig. 4.10d are the diffusivities as resulting from IR uptake experiments on crystals of the same batch. Both the absolute values and the trend in the thus determined diffusivities are in reasonably good agreement with the diffusivities derived via Eq. 2.18, since one has to take into account that the diffusivities at the highest concentration (beginning of the profiles) are determined with the highest inaccuracy due to the uncertainty in the determination of dx/dc .

Benefitting from the blockage of the 10-ring channels of the all-silica ferrierite considered in former studies, micro-imaging in [30, 71] did in turn allow a precise measurement of the methanol diffusivities along the 8-ring channels, yielding values between $10^{-13} \text{ m}^2\text{s}^{-1}$ at zero loading and close to $10^{-11} \text{ m}^2\text{s}^{-1}$ at saturation. With the present study, revealing values between $10^{-10} \text{ m}^2\text{s}^{-1}$ and $3 \times 10^{-9} \text{ m}^2\text{s}^{-1}$ for the diffusivities along the 10-ring channels, the anisotropy factor $D_{10\text{-ring}}/D_{8\text{-ring}}$ for methanol diffusion in all-silica-ferrierite is thus found to attain three orders of magnitude!

4.3 AFM Investigation of FER Surfaces

IFM sorption experiments with methanol in large ferrierite crystals of the all-silica form have shown a strong hindrance of the mass transport through the 10-ring channels of the main body of the crystal while the mass transport through the entrances of the 10-ring channels located at the triangular roof-like parts and through the 8-ring channels seems to be essentially unaffected. This effect and the removal of the transport hindrance via NaOH etching have already been discussed in section 4.2.2; this section will focus on the investigation of the etched and as-synthesized crystal surfaces via atomic

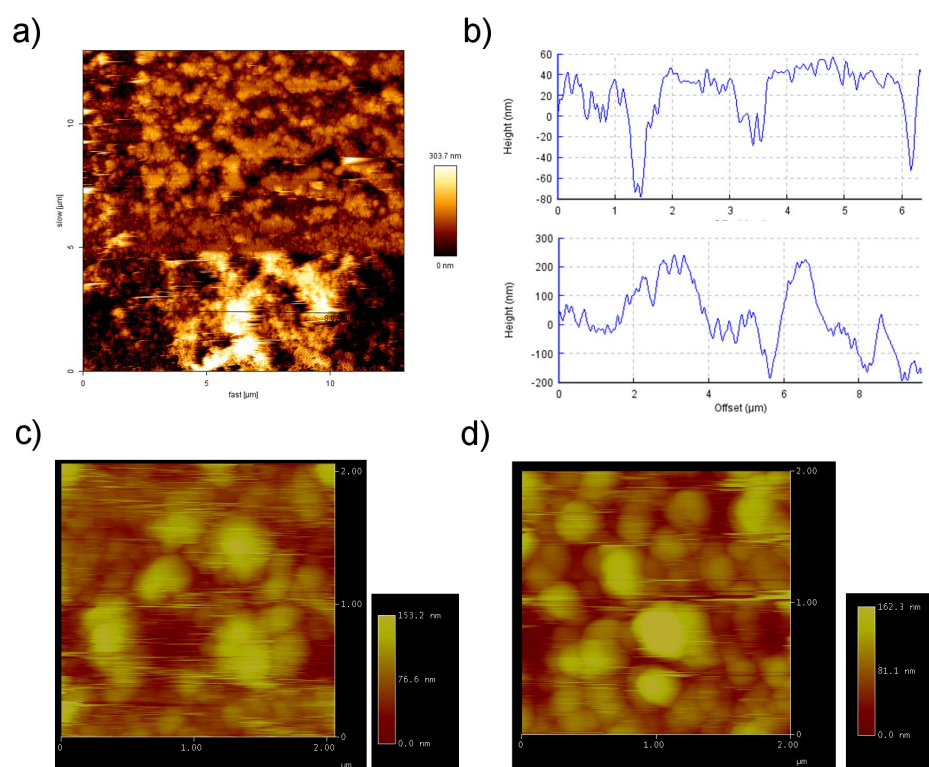


Figure 4.11: AFM micrographs of the surfaces of as-synthesized ferrierite crystals. (a) Large surface on the roof-like part of the crystal. The surface in the upper part of the picture was grinded for about an hour while the surface in the lower part was kept untouched. (b) Altitude plotted along a line in *fast*-direction of (a) in the grinded region (*top*) and the untouched region (*bottom*). (c) Surface perpendicular to the direction of the 8-ring channels. (d) Surface at the tip of the crystal.

force microscopy (AFM).

The AFM measurements presented here were carried out in collaboration with Prof. Michael Anderson and under guidance of Dr. Pablo Cubillas in the *Centre for Nanoporous Materials, School of Chemistry at the University of Manchester*. For both samples - the as-synthesized and the NaOH etched material - all three different surfaces (the large surface of the roof-like parts, the smaller surface at the sides and the surface at the tip of the crystals, see Fig. 4.9) that contribute to mass transport were investigated. The recorded micrographs are displayed in Fig. 4.11 and 4.12. Figure 4.11 summarizes the results obtained on the as-synthesized sample. All surfaces of the as-synthesized crystal are covered with a rough layer of unknown material (see Fig. 4.11c and d and on the bottom of Fig. 4.11a and b). This layer has a thickness of several dozens of nanometers and is very persistent to physical

manipulation. It could not be removed by grinding the surface with the tip of the atomic force microscope for about an hour. The effects of the grinding procedure on the surface are shown in Fig. 4.11a and b in one- and two-dimensional altitude profiles: The overall roughness of the surface is reduced but only due to the removal of the highest peaks that stick out of the surface. These peaks are chopped off while the valleys still exist in the surface landscape: The genuine surface of the material could not be reached during the grinding process.

The observations suggest that the surface layer is strongly attached to the genuine (ideal or textbook-like) surface of the crystal. Since the transport hindrances supposed to be induced by this layer were observed already right after the synthesis of the material, it seems likely that the layer was created during the synthesis process. It is thinkable that the layer consists of amorphous silicious material that was created at the end of the synthesis due to an over-saturation of the synthesis solution.

In contrast to the surfaces of the as-synthesized crystals, the surfaces of the NaOH etched crystals are much smoother and cleaner (Fig. 4.12) and allow therefore the closer examination of the surfaces structure. The surfaces at the tip of the crystal and perpendicular to the direction of the 8-ring channels are flat and bare of any distinctive features (see Fig. 4.12a and b). Plotted along a line parallel to the *fast*-axis of the two-dimensional micrograph, the altitude swing is only around one nanometer and seems to be random.

On the surface of the roof-like part of the crystal growth steps and dislocations, commonly related to defects in the crystal structure, have become visible (Fig.4.12(c)). The observed step-height is about 1 nm. This value corresponds best to the half *a*-value of the FER unit cell ($a = 1.9$ nm, $b = 1.43$ nm, $c = 0.754$ nm) or - in other words - to the *thickness* of a 10-ring channel. However, the slope derived from the observed steps ($1 \text{ nm}/1 \mu\text{m}=0.001$) is by one order of magnitude smaller than the slope typically observed with the roof-like part being of the order of 10^{-2} . The reason for that deviating observation might be that there are numerous dislocations on the crystal surface leading to smaller step length and thus to a larger slope.

The AFM micrographs have shown that the surfaces of as-synthesized and NaOH-etched crystals are of significantly different nature. While the surfaces of the as-synthesized material are rough (in terms of AFM, that means by several dozens of nanometers), the surfaces of the NaOH-etched material are clean and smooth and uncovered. But, although the surface textures of the non-etched material surfaces are similar, their effect on mass transport is notably different: while the surfaces at the roof-like parts of the crystal and the surfaces perpendicular to the direction of the 8-ring channels

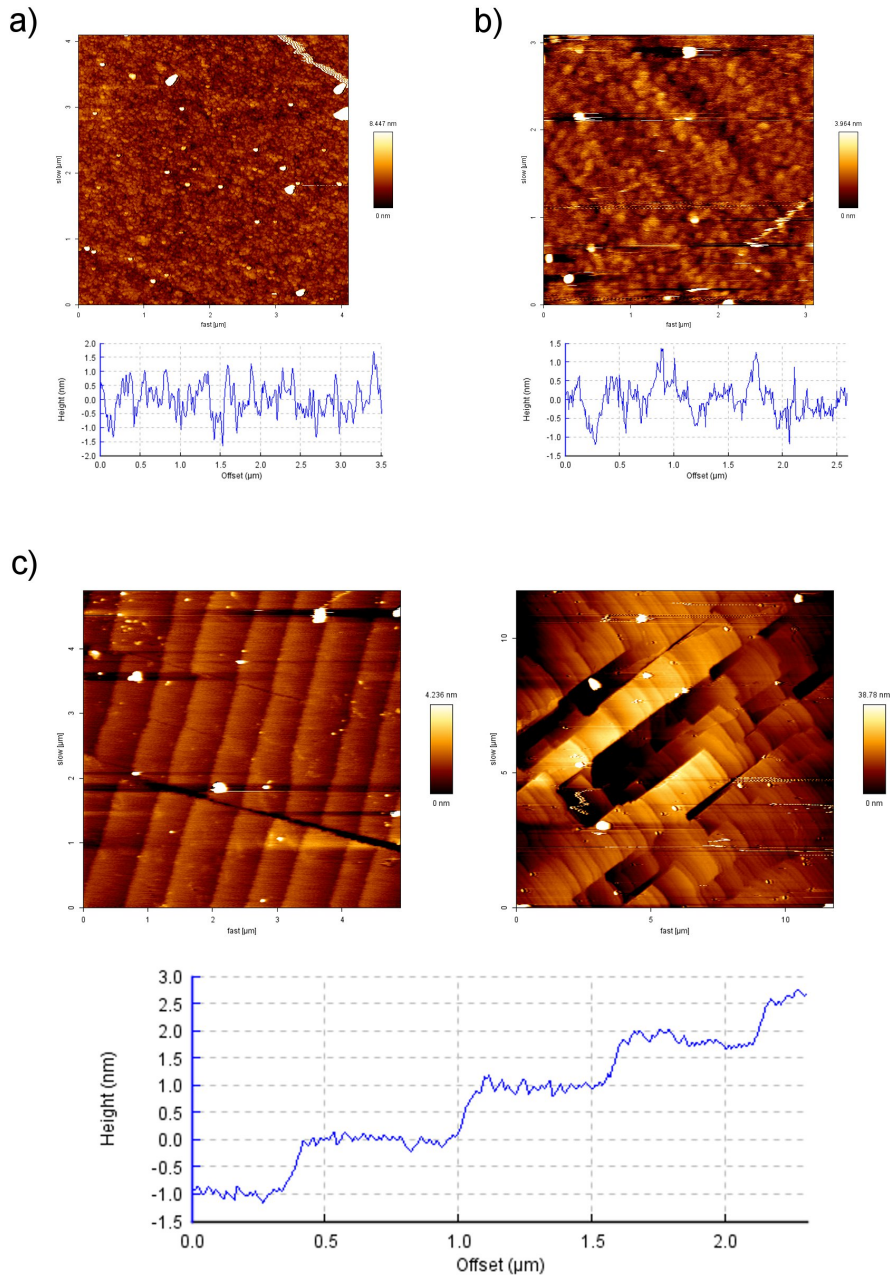


Figure 4.12: AFM micrographs and altitude-distance curves of the surface perpendicular to the 8-ring channel direction (a), of the tip (b) and of the surface of the roof-like part (c) of a NaOH etched ferrierite crystal.

are open for mass transport, the surface at the tip of the crystal is blocked to a large extend.

Furthermore, also the effects of etching are different. Again a similar effect (removal of the layer) on all three surfaces is observed, but, while the permeability at the tip of the crystal increases dramatically up to a point where its influence on mass transport is negligible, this is not observed for the other surfaces.

According to these observations, it must be concluded that, at least in the case of ferrierite, the mere existence of an additional surface layer (as observed on the as-synthesized material) does not automatically affect the mass transport through a certain surface to a significant and detectable extent. Other factors, such as the atomistic structure of the surfaces might also be of great importance for the magnitude and existence of transport barriers.

4.4 Other Molecules in Ferrierite

4.4.1 Overview

In addition to in depth uptake and release experiments with methanol in single all-silica ferrierite crystals produced by Marthala *et al.* [82], screening experiments with other small hydrocarbons (ethanol, ethane, propylene, propane and propanol) were carried out which should answer the questions *if* and *on which time scale* these molecules would be adsorbed in the crystals. In Fig. 4.13a the uptake curves for methanol, ethanol, ethane and propylene measured in single crystals of similar size are plotted which were calculated from two-dimensional concentration profiles measured with IFM via Eq. 2.3. The uptake of propane and propanol was too slow to yield meaningful profiles in reasonable time (several hours) although it was possible to observe the uptake of very small amounts of material at the edge of the crystals, but not in the center, indicating a strong diffusion hindrance for the molecules.

Even if deviations of the crystals size and the relative loading-step used in the experiments with different molecules are taken into account carefully, the large differences in the time scales of the uptake processes are clearly visible. For all molecules the uptake was two-dimensional and in principle followed the same pattern as in the case of the already discussed uptake of methanol, indicating that the NaOH treatment has worked on all studied crystals and for all guest molecules used. The shape of the profiles, in particular the clearly visible strong curvature, indicate that the uptake process is controlled by the diffusion properties of the system rather than by the permeation step on the surface.

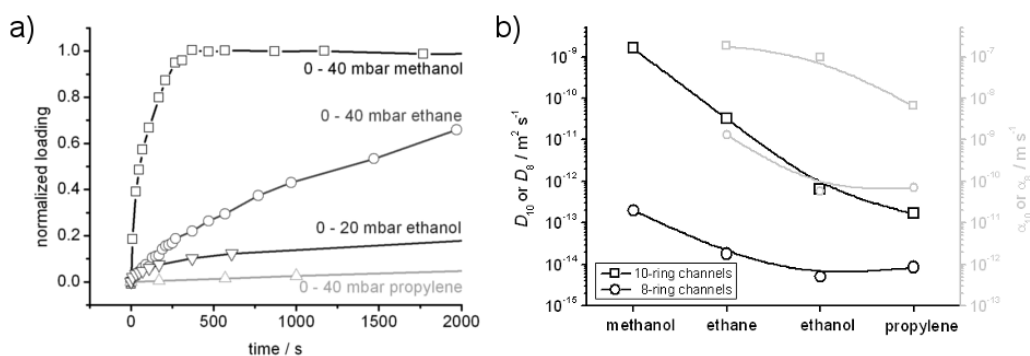


Figure 4.13: a) Integral uptake curves for the adsorptions of methanol, ethane, ethanol and propylene in single all-silica ferrierite crystals measured via IFM. The time constants of the uptake process increase from 83 s (methanol) over 1650 s (ethane) and 96000 s (ethanol) to 114000 s (propylene). The uptake of reasonable amounts of larger molecules (e.g. propane and 1-propanol) was not observed after 2-3 days. b) Transport diffusivities and surface permeabilities at zero loading.

Table 4.2 and Fig.4.13b summarize diffusivity and permeability data derived via the fitting procedure introduced in section 2.4.2 from the measured profiles. For the fits only profiles in which the diffusion fronts in both channel types did not yet reach the center of the crystal were used. This approach allowed to consider the uptake in the 8-ring channels and in the 10-ring channels to be one-dimensional and basically independent of each other. Furthermore, by restricting the fit to the first profiles of each uptake process, the influence of the roof-like parts on the profiles is small enough to be neglected although minor effects on the accuracy of the calculated parameters should be expected. The profiles were normalized to the maximum loading reached during the experiments. For ethane and propylene a pressure step of 0 - 40 mbar was used while a pressure step of 0 - 20 mbar was used in the case of ethanol.

The profiles could be fitted sufficiently with constant transport parameters except for the surface permeability in the 8-ring channels for which an exponential concentration dependence of the form $k_1 \cdot \exp(k_2 \cdot c)$ had to be used in order to catch the strong concentration dependence of the parameter. A further increase of the number of adjustable fit parameters (a more sophisticated concentration dependence) in the fit could not increase the accuracy of the fit significantly, probably due to the incompleteness of the experimental data caused by the exclusion of most profiles due to the chosen criteria. In that context, the given diffusivity and permeability values might be seen as good estimation that give an impression of the general behavior of the material rather than being absolutely accurate.

Guest Molecule	Transport Diffusivity		Surface Permeability	
	channel type	$k_0/ \text{m}^2 \text{s}^{-1}$	$k_0/ \text{m s}^{-1}$	k_1
ethane	10	3.2×10^{-11}	1.8×10^{-7}	–
	8	1.8×10^{-14}	1.3×10^{-9}	4.2
ethanol	10	6.4×10^{-13}	9.7×10^{-8}	–
	8	4.8×10^{-15}	5.8×10^{-11}	4.2
propylene	10	1.7×10^{-13}	6.5×10^{-9}	–
	8	8.5×10^{-15}	7×10^{-11}	4.5

Table 4.2: Fitting parameters used for the analytic representation of the concentration dependence of the intra-crystalline transport diffusivities D and of the surface permeabilities α for ethane, propylene and ethanol in 8- and 10-ring channels of all-silica ferrierite. The measured profiles could be fitted sufficiently with constant transport parameters except for the surface permeability of the 8-ring channels which could be described by a concentration dependence of the form $k_0 \cdot \exp(k_1 c)$.

However, the general trend for diffusion of small molecules in all-silica ferrierite is quite clear: all relevant transport parameters (diffusivities and permeabilities in(to) both channels) decrease with increasing critical diameter d_{crit} of the guest molecules, following in this way the often observed trend that the closer the molecule size gets to the channel size, the smaller gets the diffusivity.

4.4.2 Pre-Sorption of Ethanol

In the former chapter and sections a model for surface barriers on MOF Zn(tbip) and a procedure for the reduction of surface barriers on ferrierite crystals via NaOH etching were discussed. In principle these are the most interesting points when talking about surface barriers (surface barriers, not sealing of surfaces). Barriers reduce the performance of a material and are therefore generally taken to be bad for a process. In that scheme, knowledge about surface barriers is – ironically – gathered in order to reduce or, even better, remove them.

In this section I want to discuss a series of experiments that are, on the one hand, the first successful examples of multi-component experiments with interference microscopy and on the other hand some of the rare experiments that aimed in the enhancement of surface barriers rather than in their reduction.

These experiments were enabled by the large difference between the time scales of methanol and ethanol uptake in all-silica ferrierite (especially in the 8-ring channels). While the uptake of methanol is usually very fast, ethanol uptake was observed to be so slow that even after several (six) hours

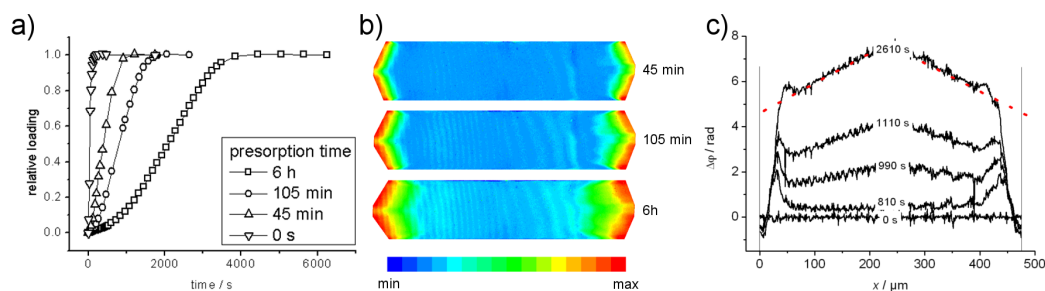


Figure 4.14: a) Uptake curves of methanol (pressure step 0 – 40 mbar methanol) measured after different pre-sorption times (45 min, 105 min and 6 h) of ethanol. b) Ethanol distribution in all silica ferrierite after adsorption times of 45 min, 105 min and 6 h (pressure step 0 – 20 mbar ethanol). c) Measured apparent concentration during the adsorption of 0 - 40 mbar methanol after 105 min of 0 - 20 mbar ethanol pre-sorption along the 10-ring channels.

of adsorption the diffusion front in the 10-ring channels did not reach the center of the crystals and no uptake was detectable in the 8-ring channels (see Fig. 4.14b), meaning that the diffusion front in the 8-ring channels at that time did not reach further into the crystal than the spatial resolution of the microscope ($0.5\ \mu\text{m}$). A total blockage of the 8-ring channels for ethanol could be excluded as uptake was indeed detected after longer time spans. However, this constellation makes it possible to study the transport of methanol in the 8-ring channels in the presence of ethanol or, more precisely, through a thin barrier of ethanol molecules 'trapped' inside the FER structure. As ethanol is by many orders of magnitude slower than methanol, previously adsorbed (pre-sorbed) ethanol molecules would be experienced by the much faster methanol molecules as static blockages of single cavities or windows in the 8-ring channels.

Figure 4.14a shows uptake curves measured during the adsorption of 0 - 40 mbar methanol after ethanol was adsorbed previously for different times (pre-sorption, pressure step 0 - 20 mbar). This was done by exchanging the complete gas phase in the vacuum-system at the beginning of the methanol adsorption. Although the physical meaning of these curves is limited due to the fact that they show the superposition of methanol uptake (via both channels) and simultaneous ethanol release (mainly via the 10-ring channels), the deceleration of the overall uptake process is clearly visible. A more precise understanding of this observation can be achieved by looking into the concentration profiles along the 10- and 8-ring channels separately (see and Fig. 4.15a, b, d, e).

In 10-ring channel direction (Fig. 4.14c) the measured profiles of the apparent concentration are strongly distorted by the superposition of simul-

taneous methanol adsorption and ethanol desorption, leading to regions in the concentration profiles in which the measured profiles underestimate the (equilibrium) concentration expected due to the crystal shape (indicated by the *dotted* red line in Fig. 4.14c) or becomes even negative, and to regions in which the measured concentration seems to exceed the maximum concentration possible in the experiment. This strange behavior is observed due to the working principle of interference microscopy in the former mentioned regions. The change of the refractive index due to the desorbed ethanol molecules is higher than the change of the refractive index caused by the adsorbed methanol molecules. This is vice versa in the latter mentioned regions where ethanol molecules that diffuse further into the ferrierite crystal add to the change of the refractive index.

The situation along the 8-ring channels is less complicated as illustrated in Fig. 4.15a, b, d and e. Since no uptake could be observed during pre-sorption, the desorbing ethanol does not disturb the methanol profiles. As visible in Fig. 4.15 the effects of pre-sorbed ethanol are similar to those of adjustable surface barriers: with increasing pre-sorption time the surface concentration at comparable times after the start of the methanol adsorption becomes smaller, which is - according to Eq. 2.15 - equivalent to an increasing surface barrier. In the common picture of surface barriers (section 3.3), a barrier is caused by a thin layer of thickness l_{barr} and reduced diffusivity D_{barr} , leading to a surface permeability $\alpha = D_{\text{barr}}/l_{\text{barr}}$. In the present case of pre-sorbed ethanol molecules this picture can also be used, but here there is no reason to assume a strong reduction of the methanol diffusivity with increasing pre-sorption time of ethanol. Instead, the thickness of the barrier increases as the pre-sorbed ethanol molecules will have traveled further into the crystal with ongoing time.

The surface permeabilities derived for pre-sorption times of 45 min, 105 min and 6 h are plotted in Fig. 4.15c for the covered apparent concentration range in which α depends almost mono-exponentially on the methanol concentration. The permeability values estimated for zero loading are plotted in Fig. 4.15f versus the square-root of the pre-sorption time t_{pre} which can be assumed to be proportional to the thickness of the pre-sorbed ethanol layer if an ideal adsorption profile for ethanol is assumed.

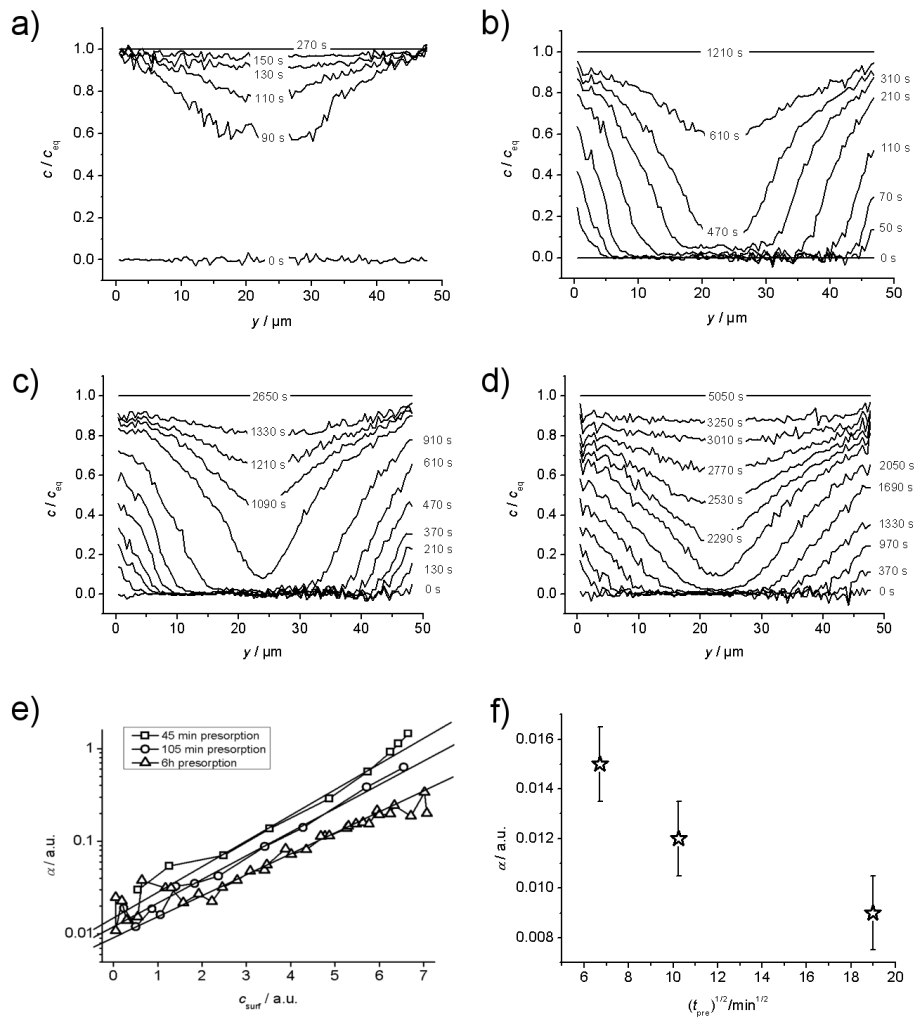


Figure 4.15: Concentration profiles in y -direction (8-ring channels) measured during the adsorption of 0 – 40 mbar methanol after different times of ethanol pre-sorption. a) no pre-sorption. b) 45 min. c) 105 min. d) 6 h. e) Surface permeability as calculated from the profiles. f) Surface permeability of methanol at zero loading versus the square-root of the ethanol pre-sorption time.

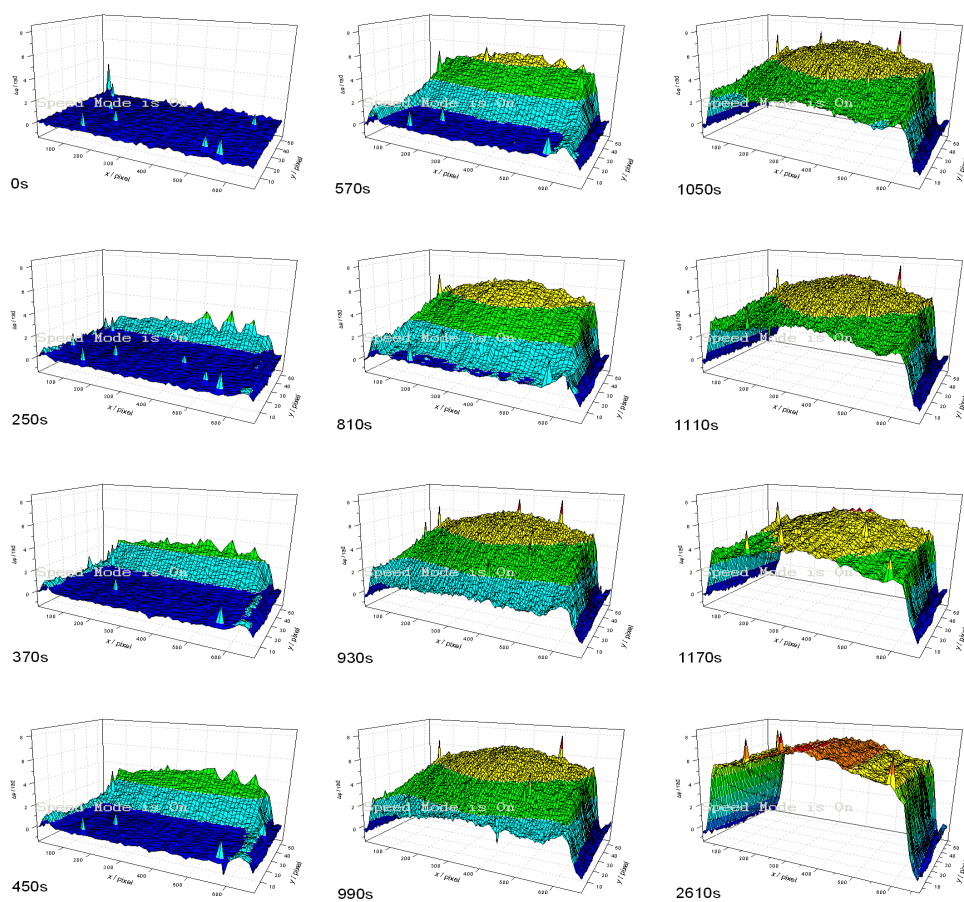


Figure 4.16: Adsorption profiles (pressure step 0 - 40 mbar) of methanol detected after 105 minutes of ethanol pre-sorption. Only half of the profiles (from $y = 0$ to $y = l_y$) are plotted to allow easier imagination of the guest molecule distribution inside the crystal.

Chapter 5

AIPO-LTA

5.1 LTA in AIPO Form

5.1.1 LTA and other 8 Member Ring Materials

Zeolites of type LTA [52] are one of the most prominent and widely used zeolite materials. The LTA pore system is three-dimensional and isotropic and consists of large cavities which are connected by narrow windows in all six spatial directions (Fig. 5.1b). The window diameter is about 4 Å and depends on the exact chemical composition (see Table 5.1). LTA can be synthesized in aluminum-silicon form (typically called zeolite A then), in pure silicon form (ITQ-29) and lately in aluminum-phosphor form (AIPO) as used in the experiments discussed here [93]. Tunable window diameter and chemical composition make LTA type materials excellent candidates for technical separation processes since guest molecule diffusivities in cavity type materials is strongly influenced by ratio of window diameter and the critical (minimal) diameter of the guest molecule [5, 94]. As a rule of thumb, the closer the critical diameter of the guest molecule comes to the window diameter, the smaller becomes the transport diffusivity and the stronger the diffusivity depends on concentration.

Material	diameter / Å	Material	diameter / Å
AIPO-LTA	3.78×3.94	ITQ-29 (Si LTA)	4.2×4
NaCa-LTA	4.6×4.2	CHA	4.1×3.9
SAPO-34	4.3×3.8	ALPO-34	4.5×3.7
DDR3R	4.4×3.65	SiCHA	4.2×3.7

Table 5.1: Summary minimum and maximum pore diameters of LTA materials of different chemical composition and other 8 member ring zeolites [95].

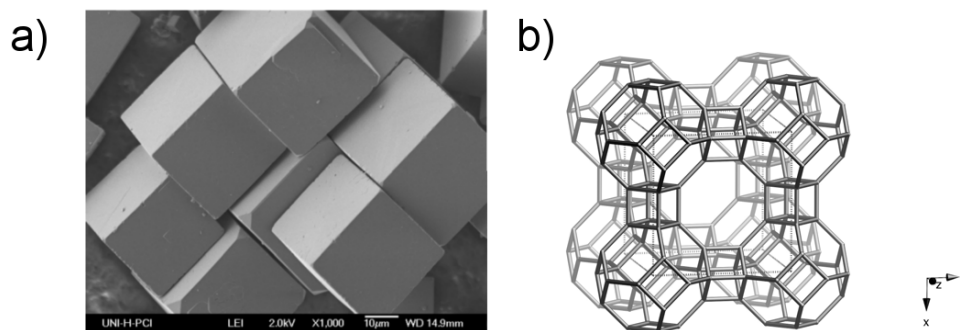


Figure 5.1: a) ALPO-LTA crystals as used in the experiments. The crystals are cubic with edge length of up to $75 \mu\text{m}$. b) Illustration of the LTA super cage. The cage can be accessed via 8-ring windows from all 6 spacial directions. The formed pore network is three-dimensional and isotropic.

5.1.2 Template Removal in ALPO-LTA

The ALPO-LTA single crystals were prepared according to the procedure reported in [96]. The habit of the thus produced crystals is shown in Fig. 5.1a. Prior to the diffusion studies, the as-made ALPO-LTA single crystals were calcined over a time span of 6 h at either 823 K in air (batch 1) or at 573 K in O_3/air (with about 100 ppm of O_3 in air, batch 2), for removing the template Kryptofix 222 used during synthesis. With both samples heating and cooling occurred at a rate of 0.2 K/min.

Crystal specimens taken from the two batches differ mainly in the amount of impurities and cracks. When calcined in air (batch 1), TG/DSC studies (Setaram Setsys 1750 Evolution) show an explosion-like combustion of the template at 690 K which causes the cracks shown in Fig. 5.2a. However, because of oxygen deficiency, thermal decomposition of the template results in carbonaceous deposits (see Fig. 5.2a). The residual carbon content was about 2 %wt and virtually all crystals in batch 1 were cracked. Temperatures of about 970 K are necessary for complete combustion of these carbon deposits. A mostly crack-free ALPO-LTA material without carbon residues is obtained by a milder de-templating procedure using an air/ozone mixture (batch 2). In situ XRD (X'Celerator with a HTK1200N heating chamber) show that the ALPO-LTA thus de-templated is stable in synthetic air and under vacuum at least up to 1200 K.

Fig. 5.2b shows a snapshot of the distribution of propylene molecules in a single crystal of batch 1 during adsorption, recorded by IFM. The impact of cracks on mass transport and molecular distribution is clearly visible: molecular concentrations increase not only starting from the external crystal surface, but also, in some crystals, from the center as a result of the presence

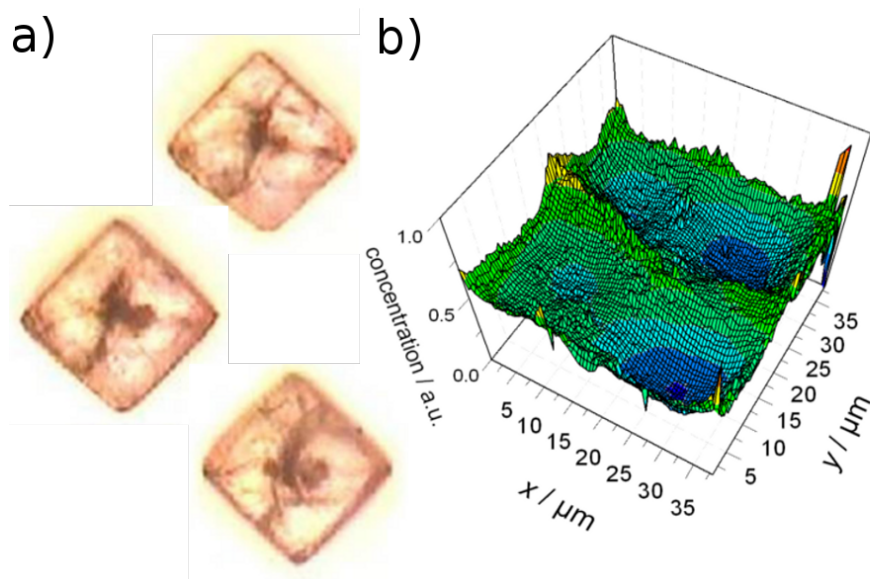


Figure 5.2: a) Micro-images of AlPO-LTA crystals of batch 1 by optical light microscopy. Template molecules that could not leave the crystal during the de-templation process were burned to carbon, causing dark spots in otherwise transparent crystals. The visible cracks were also generated during the removal of the template, most probably due to fast expansion of heated molecules. b) Typical concentration profiles recorded during propylene adsorption in crystals of batch 1 detected by IFM at 295 K. Molecular uptake is seen to occur predominantly through the cracks, corrupting diffusion studies by uptake measurement.

of cracks. In the displayed case, uptake through the cracks actually proceeds at a rate exceeding that through the external crystal surface, probably as a consequence of the creation of "fresh" surface in that region since the length, width and depth of each crack are different and impossible to determine. It is therefore impossible to quantify the influence of these cracks on molecular uptake. The focus of our micro-imaging measurements was, therefore, on the AlPO-LTA crystals of batch 2.

5.2 Investigations of Mass Transport in AlPO-LTA

5.2.1 IFM Experiments

The pore system of LTA type materials is three-dimensional and therefore not ideally structured for interference microscopy experiments as uptake occurs also in observation direction (see section 2.1). This disadvantage can be compensated by making use of the isotropy of the pore system during data analysis and by choosing the most convenient guest molecule with respect

to restrictions of the the experimental set-up. In the present case propylene turned out to be this molecule as its uptake time (below one hour per experiment) was short enough for the realization of a medium sized number of systematic experiments but at the same time still large compared to the temporal resolution of the IFM set-up so that a sufficient number of profiles could be detected during each experiment. In addition to propylene also ethane and propane were tested, but while the uptake of ethane was too fast for the detection of concentration profiles via IFM (several seconds; almost below the temporal resolution of the set-up), the uptake of propane was too slow (scales in days) for systematic experiments (Fig. 5.4).

The IFM experiments performed with propylene in AIPO-LTA single crystals are summarized in Fig. 5.3a: In a first series, the propylene pressure was increased in small steps up to a maximum pressure of 600 mbar. After each pressure step, the evolution of the intra-crystalline particle concentration till equilibrium establishment was recorded. Desorption, initiated by a stepwise decrease in the surrounding pressure, was recorded correspondingly (beginning at 250 mbar). The equilibrium concentrations reached after each small-step ad- or desorption are indicated in Fig. 5.3a as *filled* (adsorption) and *open* (desorption) squares. The obtained isotherm could be fitted with a single-site Langmuir isotherm (Eq. 2.6) resulting in a calculated maximum concentration of $c_{\max} = 3.7$ molecules per cavity and a Langmuir parameter of $k_L = 0.0115 \text{ mbar}^{-1}$. The measured (relative) IFM data was calibrated by comparison to literature data measured in the also cation-free LTA structure ITQ-29 [97, 98].

In addition, also a few ad- and desorption experiments with larger pressure steps beginning (respectively ending, in the case of desorption) at vacuum (indicated by *arrows* in Fig. 5.3a) were performed and repeated several times in order to proof the reproducibility of the experiments. In both sets of experiments the equilibrium loading was shown to be the same. In contrast to the behaviour observed with cation-containing LTA [18, 24], molecular uptake and release with one and the same crystal was found to be completely reproducible after an adsorption-desorption cycle, as exemplified by the concentration profiles measured in subsequent experiments with the same pressure step and the uptake and release curves measured in subsequent adsorption and desorption experiments plotted in Fig. 5.3b and c.

Figure 5.4 provides examples of the complete information provided by an IFM experiment, namely the two-dimensional representation of the evolution of the concentration integrals over a crystal face for the uptake of 0 - 250 mbar propylene (*middle* row of Fig. 5.4) and 0 - 250 mbar propane (*bottom* row of Fig. 5.4). It simultaneously illustrates the particularly convenient measuring conditions provided by propylene as a guest molecule. In the *top*

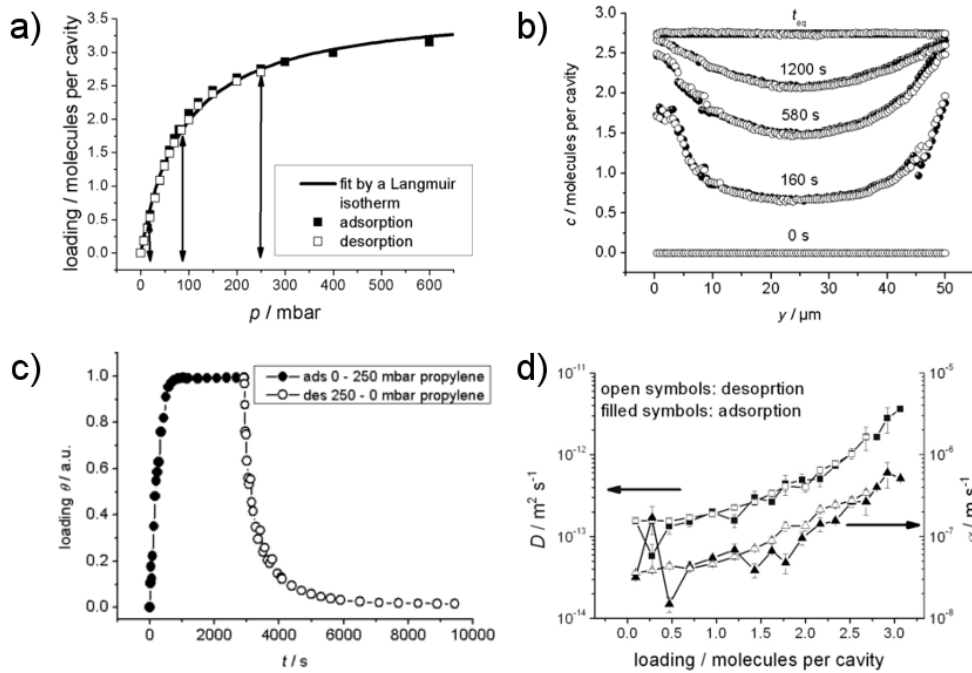


Figure 5.3: Overview of the IFM experiments with propylene in AlPO-LTA crystals of batch 2 at 295 K. a) Adsorption isotherm. Squares indicate the equilibrium loading of small-step adsorption (*full symbols*) and desorption (*open symbols*) experiments. Arrows indicate experiments with larger pressure steps (0 - 20 - 0 mbar, 0 - 100 - 0 mbar, 0 - 250 - 0 mbar). *Full line* indicates the result of a fit with Langmuir isotherm. b) IFM Concentration profiles of two subsequent sorption experiments (0 - 250 mbar propylene) through the crystal center (i.e. profiles along the central horizontal and vertical lines in the 2d-plots as shown in Fig. 5.4). c) Uptake (*full symbols*) and release (*open symbols*) curves of subsequent adsorption and desorption experiments. Unlike LTA structures with cations (NaCaA), the cation-free AlPO-LTA releases all adsorbed material. d) Transport diffusivities D (squares) and surface permeabilities α (triangles) of propylene in AlPO-LTA at 295 K, calculated from the transient concentration profiles recorded by IFM during molecular uptake following stepwise pressure change.

row of Fig. 5.4 concentration profiles calculated using the analytical solution of Fick's laws for uptake in a cube of edge-length $2l$ with constant diffusivity and surface permeability [64] (Eq. 2.19) are plotted for $D = 3 \times 10^{-13} \text{m}^2 \text{s}^{-1}$ and $\alpha = 2 \times 10^{-7} \text{m s}^{-1}$. These values were chosen to demonstrate the close agreement between the theoretically predicted and experimentally observed concentration patterns. Small differences between the measured and simulated profiles can be attributed to the simplifying use of constant diffusivity and permeability values in the simulations as well as to possible deviations from crystal regularity and to the noise inherent to all experimental measurements. The last two reasons also explain the small deviations in the measured profiles from ideal symmetry.

The comparison between propane and propylene yields two important differences. First Fig. 5.4 illustrates the different time scales of the transient sorption experiments with propylene (minutes) and propane (time spans over days). Due to the inconvenient adsorption time for propane, only one experiment, adsorption from 0 – 250 mbar, was performed. A mean diffusivity ($2 \times 10^{-15} \text{m}^2 \text{s}^{-1}$) for this uptake process was estimated by fitting the uptake curve with Eq. 2.17. As the second remarkable difference, the concentration profiles recorded during propane adsorption are found to deviate much more strongly from symmetry than those obtained with propylene on one and the same crystal. These deviations are particularly pronounced during the initial stage of uptake, when the influence of the surface resistances is particularly significant. It is most likely, therefore, that the surface permeability is not absolutely homogeneous for propane as implied in data analysis for propylene, but locally differing. This explanation would nicely correspond with the fact that the critical diameter of propane is closer than that of propylene to the window diameter.

The intra-crystalline transport diffusivity and the surface permeability for propylene, are obtained by considering the concentrations resulting from the solution of the diffusion equation for uptake by a cube of the extension $(2l)^3$ (Eq. 2.19). The diffusivity and the surface permeability were varied independently to yield the best fit between the integrals of the calculated concentrations and those measured by IFM. As the individual loading steps of each individual small-step uptake (or release) experiment were small compared to the possible maximum loading, both, the diffusivity and the surface permeability were assumed to be constant as implied by Eq. 2.19 in each fit. The resulting data is shown in Fig. 5.3d.

Transport diffusivities and surface permeabilities, are found to vary with concentration in exactly the same way over more than an order of magnitude, a pattern also observed for short-chain alkanes in MOF Zn(tbip) (see chapter 3) [40, 73] which has given rise to a new picture of the nature of

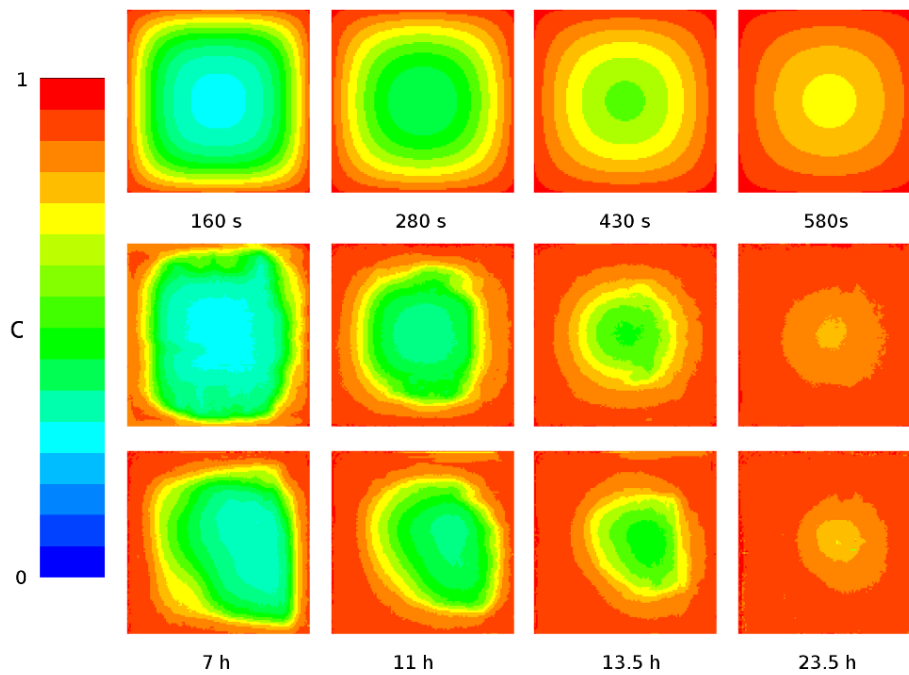


Figure 5.4: IFM profiles of the concentration integrals perpendicular to a crystal face during three-dimensional uptake of propylene (*middle*) and propane (*bottom*) in one and the same crystal of AlPO-LTA after a pressure step from zero to 250 mbar at 295 K and their representation for an ideal cubic structure (*top*) as following with the analytical expressions of intra-crystalline concentration (Eq. 2.19) determined by assuming constant surface permeability ($2 \times 10^{-7} \text{ m s}^{-1}$) and intracrystalline diffusivity ($3 \times 10^{-13} \text{ m}^2 \text{ s}^{-1}$).

transport resistances - the model which is discussed in section 3.3 in more detail, but in this case without the necessity of making further assumptions about the real structure of the material (as for example assuming defects in the real structure).

Here one may refer directly to the classical relation of the effective medium approach where the permeability through an impermeable boundary is given by Eq. 3.4 resulting in the following estimation for the probability of open pores at the crystal surface:

$$p_{\text{open}} \approx \frac{\alpha}{D} 2a, \quad (5.1)$$

yielding a rule of thumb for an estimate of the fraction p_{open} of unblocked surface area. The increase of this fraction, for a fixed permeability-to-diffusivity ratio, with increasing hole-diameter is a direct consequence of the correlation between D and α postulated by Dutko *et al.* (Eq. 3.3) and may easily be rationalized by realizing that, for a given value of p_{open} , the efficiency of the openings for mass transfer increases with their degree of dispersion [73].

With $\alpha/D \approx 2 \times 10^5 \text{ m}^{-1}$ as resulting from the experiments (Fig. 5.3d) and with $2a \approx 1, 2 \text{ nm}$ corresponding to the highest degree of hole dispersion (the limiting case in which, on the external surface, unblocked windows do not occur in adjacent unit cells) p_{open} is found to be of the order of 10^{-4} . This means that among several 1000 "windows" connecting the intra-crystalline space with the surroundings, only a single one is permeable. Eq. 5.1 further on indicates that, for the given permeation-to-diffusion ratio, the percentage of unblocked windows, p_{open} will become larger, when there is some "clustering" of the unblocked windows on the crystal surface.

5.2.2 In Larger Context

In Fig. 5.5 the results of IFM diffusion experiments with propylene and propane on AIPO-LTA are compared to experimental results obtained with IR microscopy and PFG NMR on diffusion of ethane on the same sample (Fig. 5.5b) [99] and with results from the literature on diffusion of the same selection of guest molecules in LTA material of other chemical composition (ITQ-29 (Fig. 5.5c) and NaCa LTA (Fig. 5.5a), measured by PFG NMR [97, 98], ZLC [100].

The data confirm the observation that guest diffusion in the cation-free LTA isomorphs [101] is notably slower than in Ca-containing LTA [97, 98]. It is remarkable that, even for ethane, for which the critical diameter (3.7 \AA) is substantially smaller than the free diameter of the 8-ring, the diffusivities in NaCa LTA and ITQ-29 differ by one order of magnitude. Hindrance of

rotation in the transition state offers a possible explanation. In cationic LTA the effect of the window dimensions is complicated by the presence of bivalent calcium cations which are known to reduce the diffusivity of the guest molecules especially for unsaturated species [91]. This probably explains the coincidence of the diffusivities for propane and propylene (which is slightly smaller) in CaA, as shown in Fig. 5.5a. However, in the cation free samples, the observed decrease in the diffusivities must clearly be ascribed to the reduction in the window dimensions. In conformity with this conclusion, the reduction of the diffusivity is most pronounced for propane which has the largest critical diameter of all guest molecules considered.

The effect of the window dimensions on the diffusion of small molecules in 8-ring zeolites has been studied in some detail experimentally, especially for the CHA family [95, 97, 98], but also more generally for various structure types by computer simulations [94]. The authors conclude similarly that the diffusivity of guest molecules depends drastically on the ratio of (critical) molecule diameter and window diameter, leading to a strong reduction of the diffusivity if the ratio goes to unity. Experimental diffusivity data for propylene, ethylene and methane from several different sources are summarized in Figure 5.6. The diffusivities correlate closely with the minimum diameter of the 8-ring. It is clear that the variation is dramatic, spanning three orders of magnitude for propylene, with an especially sharp decline when the minimum ring diameter reaches the critical molecular diameter ($\approx 3.75 \text{ \AA}$).

The synthesis of large crystals of cation-free zeolites of type AIPO-LTA with perfect crystal habit has allowed detailed diffusion studies of nanoporous host materials with three-dimensional pore-networks by micro-imaging. The cubic symmetry of the host material allows a so far unattained accuracy in the measurement of both the intra-crystalline diffusivities and surface permeabilities, as demonstrated in an in-depth study with propylene as a guest molecule.

Notably, over concentration ranges where both the surface permeability and intra-crystalline diffusivity varied over more than an order of magnitude, their mutual ratio was found to remain constant, similar to the behavior observed for light hydrocarbons in the one-dimensional pore network of Zn(tbip) (chapter 3). These observations again provide strong support for the view that, at least for these systems, the surface resistance arises from complete blockage of most of the pore entrances rather than from the presence of a more or less uniform surface layer with a substantially reduced permeability.

By comparing the experimental results obtained by interference microscopy with those obtained by IR micro-imaging and PFG NMR as alternative, complementary "microscopic" techniques for diffusion measurement, the understanding of the behavior of AIPO-LTA was extended to guest molecules of

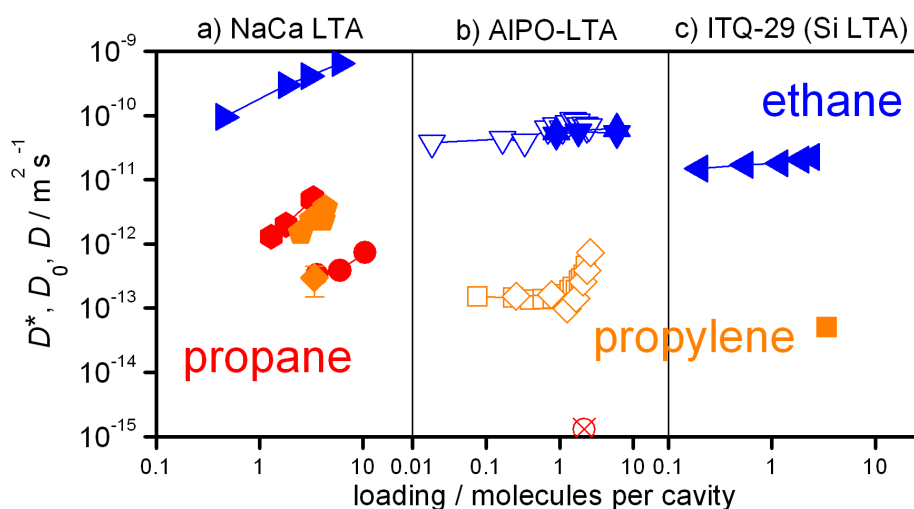


Figure 5.5: Diffusivities (full symbols: self-diffusivities; open symbols: corrected diffusivities) of ethane (triangles), propylene (squares and diamonds) and propane (circles) at room temperature (298 K) in different LTA-type zeolites determined by microscopic measuring techniques: (a) Na(75)CaA (NaCa LTA): PFG NMR self-diffusivities of ethane (\blacktriangleleft , [102]), propylene (\blacklozenge , [98]) and propane (\bullet , [102]) and ZLC/TZLC Data for propane (*hexagon*) and propylene (*pentagon*) in CaA (approx 75% exchanged) at 358 K [100]; (b) AIPO-LTA (this study): PFG NMR self-diffusivities of ethane in batch 1 (\blacktriangle) and batch 2 (\blacktriangledown) and corrected (transport) diffusivities of ethane in batch 2 (\triangleright), corrected (transport) diffusivities of propylene in batch 2 resulting from IFM (\square) and IRM (\diamond) and transport diffusivity of propane in batch 2 (\otimes); (c) ITQ-29 (Si LTA): PFG NMR self-diffusivities of ethane (\blacktriangleleft , [98]) and propylene (\blacksquare , [97])

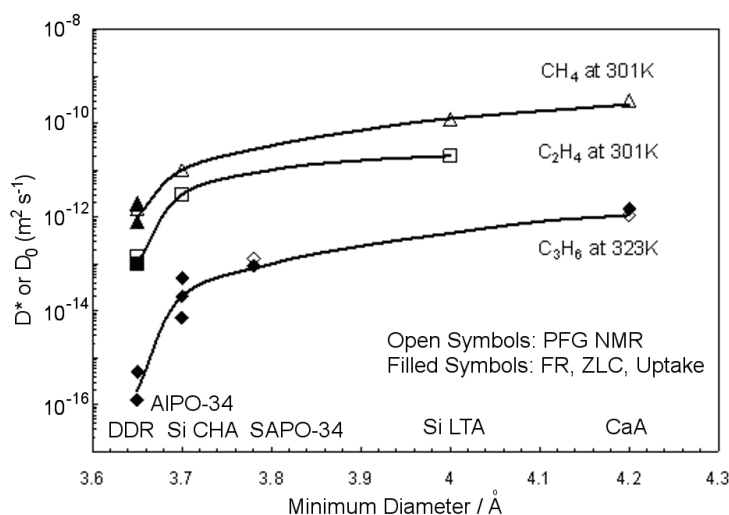


Figure 5.6: Correlation of diffusivity data for light hydrocarbons in 8-ring zeolites with minimum window diameter [103].

both higher (ethane) and lower (propane) diffusivities.

As a general feature of all these studies, the diffusivities of guest molecules in the cation-free LTA zeolites (ITQ-29 and ALPO-LTA) were found to be significantly smaller than in the cation-containing LTA-type zeolite NaCaA [102]. As originally pointed out by Hedin *et al.* this is consistent with the slight reduction of the window apertures of the Si and ALPO forms [97].

Chapter 6

Summary

The focus of this work was the investigation of mass transport via micro imaging in microporous crystalline materials and its description in terms of transport diffusion and surface permeation. Molecular transport in three different porous structures, two zeolites of structure type FER and LTA and in the metal organic framework structure Zn(tbip) was investigated via interference microscopy and analyzed analytically and via computer simulations.

The present interference microscopy setup with attached static vacuum system, thermal insulation and heating system allows a variety of adsorption and transport studies in transparent porous materials at temperatures between room temperature and 100 °C. Obtainable experimental results contain: adsorption isotherms, adsorption and desorption kinetics and, most importantly, transient concentration profiles under equilibrium and non-equilibrium conditions. One major progress in the art of experimenting via interference microscopy was the observation of first multi-component uptake experiments in FER type zeolite with this technique - a type of experiment which was formally thought to be impossible to be conducted. A second important progress was the development of a model for the description of transport barriers on crystal surfaces based on experimental result gathered in the course of the work.

MOF Zn(tbip)

Uptake curves and transient concentration profiles of propane in the one-dimensional pore network of the metal organic framework Zn(tbip) have been recorded at room temperature and elevated temperatures. Based on these experiments, activation energies for diffusion and surface permeation were calculated which were identical. This finding supported former experimental results and computer simulations that suggested that intra-crystalline diffusion and surface permeation were controlled by basically the same mechanism that was responsible for the existence of surface barriers on these crystals.

In contrast to conventional visualizations of surface barriers in the form of homogeneous layers of reduced permeability, the total blockage of (the majority of) pores at the surface was identified to be a possible explanation for the observed barriers. In addition to computer simulations this model was supported by the investigation of the crystal surfaces after long times of storage during which the surface was covered by an amorphous layer which reduced the permeability of the material surfaces.

FER-Type Zeolites

Mass transport in all-silica ferrierite was studied via the analysis of transient concentration profiles of methanol at room temperature and elevated temperatures and ethanol, ethane, propylene and propane at room temperature. Methanol uptake was studied in two different samples. For both samples a strong hindrance of uptake via the 10-ring channels of the two-dimensional pore structure was observed. After reduction of this hindrance via NaOH etching two-dimensional and anisotropic uptake could be observed with all employed guest molecules. Diffusion in 10-ring channels could be analyzed using the Boltzman-Matano method which could be applied to concentration profiles measured via interference microscopy for the first time without the need of further model assumption. The derived intra-crystalline diffusion and the surface permeability both decreased with increasing kinetical diameter of the guest molecules. In pre-sorption experiments of ethanol and methanol in ferrierite, the pre-sorbed ethanol in the 8-ring channels acted as surface barrier which increased with increasing pre-sorption time just as well as the thickness of the pre-sorbed ethanol layer.

AIPO-LTA Zeolite

Adsorption isotherms, uptake curves and concentration profiles have been measured for propylene and propane in the three-dimensional LTA pore network of the AIPO form in more than 50 adsorption and desorption experiments. The observed uptake was completely reproducible and reversible in contrast to many other reports in the literature. The derived diffusivities and surface permeabilities showed identical concentration dependence over more than one order of magnitude. This observation could be consistently interpreted with the model developed for mass transport and surface permeation from experimental results on Zn(tbip). The measured diffusivities were compared with the rich data available for diffusion of other small molecules in the various LTA realizations in the literature and were found to support once more the critical influence of molecule size in cavity type materials on diffusion and mass transport.

Conclusion

It has been shown that the unique information, which can be accessed by interference (and IR microscopy), provides an important contribution for understanding molecular transport in porous materials. Interference microscopy is one out of very few techniques that provides the experimentalist with spatial-resolved information of the guest molecule concentration and thus the exact location of regions with retarded (barriers) or enhanced (cracks) transport and the orientation of the pore network (if the transport is anisotropic).

However, interference microscopy can only observe the effects and not their causes. While it is often straight forward to correlate unexpected transport phenomena inside the porous material with the pore structure, the orientation of the pore network or the size and shape of the guest molecule, it is by far more difficult to explain surface barriers - mostly due to the fact that it is extremely difficult to achieve molecular resolution of the surface with the present imaging techniques. Nevertheless the combination of interference microscopy and imaging techniques such as AFM, SEM or TEM - as it was already tried for the first time within this work - seems to be the right approach to investigate the dubious source of the barriers, if the resolution of the mentioned techniques can be increased reliably. Currently, hypothesis on the nature of surface barriers are still limited to model assumptions based on indirect experimental observations, although it is also still possible, as presented here, to improve and modify these models solely based on the results of interference microscopy.

Bibliography

- [1] G. Ertl, H. Knözinger, F. Schüth & J. Weitkamp: *Handbook of Heterogeneous Catalysis, 2nd Edn.* (Wiley-VCH, Weinheim, 2008).
- [2] F. Schüth, K. S. W. Sing & J. Weitkamp: *Handbook of Porous Solids* (Wiley-VCH, Weinheim, 2002).
- [3] TechInsight. Zeolites: Industry trends and worldwide markets in 2010. Tech. Rep., Technical Insights Inc (2001).
- [4] D. Ruthven: *Principles of Adsorption and Adsorption Processes* (New York, 1984), wiley edn.
- [5] J. Kärger, D. M. Ruthven & D. Theodorou: *Diffusion in Nanoporous Materials* (Wiley - VCH, Weinheim, 2012).
- [6] F. Laeri, F. Schüth, U. Simon & M. Wark: *Host-Guest Systems Based on Nanoporous Crystals* (Wiley-VCH, Weinheim, 2003).
- [7] D. Ruthven: *Ind. Eng. Chem. Res.* **39**, 2127 (2000).
- [8] J. Kärger & D. Ruthven: *Zeolites* **9**, 267–281 (1989).
- [9] S. Brandani & D. Ruthven: *Chem. Eng. Sci.* **55**, 1935–1937 (2000).
- [10] H. Jobic *et al.*: *Adsorption* **11**, 403–407 (2005).
- [11] C. Chmelik *et al.*: *Chem. Phys. Chem.* **12**, 1130–1134 (2011).
- [12] D. M. Ruthven & S. Brandani: Measurement of diffusion in porous solids by zero length column (zlc) methods. In N. Kanellopoulos (ed.) *Recent Advances in Gas Separation by Microporous Ceramic Membranes*, 187–212 (Elsevier, Amsterdam, 2000).
- [13] L. Rees & L. Song: Frequency response methods for the characterization of microporous solids. In N. Kanellopoulos (ed.) *Recent Advances*

- in Gas Separation by Microporous Ceramic Membranes*, 139–186 (Elsevier, Amsterdam, 2000).
- [14] R. Barrer & B. Fender: *J. Phys. Chem. Solids* **21**, 1–24 (1961).
- [15] B. Blümich: *NMR Imaging of Materials* (Clarendon Press, Oxford, 2000).
- [16] P. Blümli, B. Blümich, R. Botto & E. Fukushima: *Spatially Resolved Magnetic Resonance* (Weinheim, 1998).
- [17] G. H. A. van der Heijden *et al.*: *Chem. Eng. Sci.* **64**, 3010–3018 (2009).
- [18] U. Schemmert *et al.*: *Micropor. Mesopor. Mat.* **32**, 101–110 (1999).
- [19] C. Chmelik: *FTIR Microscopy as a Tool for Studying Molecular Transport in Zeolites*. Ph.D. thesis, Leipzig University, Leipzig (2007).
- [20] C. Chmelik *et al.*: *Chem. Phys. Chem.* **10**, 2623–2627 (2009).
- [21] C. Chmelik *et al.*: *Chem. Eng. Technol.* **82**, 779–804 (2010).
- [22] J. Kärger: *Sitzungsberichte der Sächsischen Akademie der Wissenschaften zu Leipzig* **128 (6)**, 5–43 (2003).
- [23] J. Kärger *et al.*: *Feingerätetechnik* **27**, 539–542 (1978).
- [24] U. Schemmert *et al.*: *Europhys. Lett.* **46**, 204–210 (1999).
- [25] U. Schemmert: *Interferenzmikroskopisch Untersuchungen zur Moleküldiffusion in mikroporösen Materialien*. Phd. thesis, Leipzig University, Leipzig (2001).
- [26] O. Geier *et al.*: *J. Phys. Chem. B* **105**, 10217–10222 (2001).
- [27] E. Lehmann *et al.*: *J. Phys. Chem. B* **107**, 4685–4687 (2003).
- [28] E. Lehmann *et al.*: *J. Am. Chem. Soc.* **124**, 8690–8692 (2002).
- [29] P. Kortunov *et al.*: *Chem. Mater.* **16**, 3552–3558 (2004).
- [30] P. Kortunov *et al.*: *J. Phys. Chem. B* **110**, 23821–23828 (2006).
- [31] P. Kortunov *et al.*: *Chem. Mater.* **19**, 3917–3923 (2007).
- [32] P. Kortunov *et al.*: *J. Am. Chem. Soc.* **129**, 8041–8047 (2007).

- [33] D. Tzoulaki *et al.*: *Micropor. Mesopor. Mat.* **110**, 72–76 (2008).
- [34] D. Tzoulaki *et al.*: *Angew. Chem. Int. Ed.* **47**, 3954–3957 (2008).
- [35] D. Tzoulaki *et al.*: *Angew. Chem. Int. Edit.* **48**, 3525–3528 (2009).
- [36] D. Tzoulaki *et al.*: *J. Am. Chem. Soc.* **132**, 11665–11670 (2010).
- [37] L. Heinke & J. Kärger: *N. J. Phys.* **10**, 023035 (2008).
- [38] L. Heinke *et al.*: *Phys. Rev. Lett.* **102**, 065901 (2009).
- [39] F. Hibbe: *Interferenzmikroskopische Untersuchung der Temperaturabhängigkeit transienter Konzentrationsprofile in nanoporösen Materialien*. Diploma thesis, Universität Leipzig (2008).
- [40] F. Hibbe *et al.*: *J. Am. Chem. Soc.* **133**, 2804–2807 (2011).
- [41] C. Chmelik & J. Kärger: *Chem. Soc. Rev.* **39**, 4864–4884 (2010).
- [42] S. Han *et al.*: *Angew. Chem. Int. Edit.* **51**, 1–6 (2012).
- [43] H. Beyer & G. Schöppe: *Theorie und Praxis der Interferenzmikroskopie* (Akademie Verlag, Leipzig, 1965).
- [44] J. Rouquerol *et al.*: *Pure Appl. Chem.* **66**, 1739–1758 (1994).
- [45] T. Armbruster: Zeolites and mesoporous solids at the dawn of the 21st century. In *Studies in Surface Science and Catalysis*, vol. 135, 13 (Elsevier, 2001).
- [46] C. J. Rhodes: *Annu. Rep. Prog. Chem., Sect. C* **103**, 287 – 325 (2007).
- [47] J. Caro *et al.*: *Adsorption* **11**, 215–227 (2005).
- [48] T. C. Bowen *et al.*: *J. Membrane Sci.* **245**, 1–33 (2004).
- [49] J. van den Bergh, J. Gascon & F. Kapteijn: Diffusion in zeolites – impact on catalysis. In J. Cejka, A. Corma & S. Zones (eds.) *Zeolites and Catalysis: Synthesis, Reactions and Applications* (Wiley, 2010).
- [50] A. F. v. Cronstedt: *Akad. Handl. Stockholm* **17**, 120–123 (1756).
- [51] R. Barrer: *J. Chem. Soc.* 2158–2163 (1948).
- [52] C. Baerlocher, L. B. McCusker & D. H. Olson: *Atlas of Zeolite Framework Types* (Elsevier, Amsterdam, 2007), 6 edn.

- [53] C. Gücüyener *et al.*: *J. Am. Chem. Soc.* **132**, 17704–17706 (2010).
- [54] G. Vogl: *Wandern ohne Ziel: Von der Atomdiffusion zur Ausbreitung von Lebewesen und Ideen* (Springer, Berlin, Heidelberg, 2007).
- [55] A. Einstein: *Ann. Phys.* **17**, 549–560 (1905).
- [56] A. Fick: *Ann. Phys. Chem.* **94**, 59–86 (1855).
- [57] C. Chmelik *et al.*: *Phys. Rev. Lett.* **104**, 085902 (2010).
- [58] I. S. Anastisios & D. S. Sholl: *J. Phys. Chem. B* **105**, 3151–3154 (2001).
- [59] J.-M. Simon *et al.*: *J. Phys. Chem. B* **109**, 13523–13528 (2005).
- [60] D. M. Ford & E. D. Glandt: *J. Phys. Chem.* **99**, 11543–11549 (1995).
- [61] D. M. Ford & E. D. Glandt: *J. Membrane Sci.* **107**, 47–57 (1995).
- [62] A. Jentys *et al.*: *J. Phys. Chem. B* **2006**, 17691 (2006).
- [63] N. E. R. Zimmermann *et al.*: *J. Phys. Chem.* **116**, 3677–3683 (2012).
- [64] J. Crank: *The Mathematics of Diffusion* (Clarendon Press, Oxford, 1975).
- [65] J.-R. Li *et al.*: *Chem. Soc. Rev.* **38**, 1477–1504 (2009).
- [66] K. Hahn *et al.*: *Phys. Rev. Lett.* **76**, 2762–2765 (1996).
- [67] P. S. Burada *et al.*: *Chem. Phys. Chem.* 45–54 (2009).
- [68] J. Kärger: Single-file diffusion in zeolites. In H. G. Karge & J. Weitkamp (eds.) *Molecular Sieves, Science and Technology: Adsorption and Diffusion*, vol. 7, 329–366 (Springer, Berlin, 2008).
- [69] C. Chmelik *et al.*: *Micropor. Mesopor. Mat.* **129**, 340–344 (2010).
- [70] D. Reed & G. Ehrlich: *Surf. Sci.* **102**, 588 (1981).
- [71] J. Kärger *et al.*: *Angew. Chem. Int. Edit.* **45**, 7846–7849 (2006).
- [72] O. K. Dudko *et al.*: *J. Phys. Chem. B* **109**, 21296–21299 (2005).
- [73] L. Heinke & J. Kärger: *Phys. Rev. Lett.* **106**, 74501 (2011).
- [74] D. S. Sholl: *Nature Chemistry* **3**, 429–430 (2011).

- [75] O. K. Dudko *et al.*: *J. Chem. Phys.* **121**, 11283–11288 (2004).
- [76] C. Tuck: *Effective Medium Theory* (Oxford University Press, Oxford, Oxford, 1999).
- [77] L. Heinke & J. Kärger: *Diffus. Fundam.* **9**, 2.1 (2008).
- [78] P. Kortunov *et al.*: *Adsorption* **11**, 235–244 (2005).
- [79] L. Heinke *et al.*: *Chem. Eng. Technol.* **30**, 995–1002 (2007).
- [80] F. Hibbe *et al.*: *Chem. Ing. Tech.* **83**, 2211–2218 (2011).
- [81] L. Heinke *et al.*: *Europhys. Lett.* **81**, 26002 (2008).
- [82] V. R. R. Marthala *et al.*: *Chem. Mater.* **11**, 2521 (2011).
- [83] R. A. Rakoczy *et al.*: *Micropor. Mesopor. Mat.* **104**, 1195–1203 (2007).
- [84] H. G. Karge & J. Kärger: Application of ir spectroscopy, ir microscopy, and optical interference microscopy to diffusion in zeolites. In H. Karge & J. Weitkamp (eds.) *Adsorption and Diffusion*, vol. 7 of *Molecular Sieves, Science and Technology*, 135–206 (Springer, Berlin, Heidelberg, 2008).
- [85] R. Krishna *et al.*: *Chem. Soc. Rev.* **31**, 185–194 (2002).
- [86] R. Krishna: *J. Phys. Chem. C* **113**, 1975619781 (2009).
- [87] L. Heinke & J. Kärger: *J. Chem. Phys.* **130**, 044707–1–8 (2009).
- [88] F. Keil *et al.*: *Rev. Chem. Engin.* **16**, 71–197 (2000).
- [89] J. Kärger & H. Pfeifer: *Zeolites* **7**, 90–107 (1987).
- [90] R. Krishna & J. M. van Baten: *Micropor. Mesopor. Mat.* **125**, 126–134 (2009).
- [91] W. Heink *et al.*: *Zeolites*. **14**, 320–325 (1994).
- [92] Bronstein, Semendjajew, Musiol & Mülig: *Taschenbuch der Mathematik* (Harri Deutsch, Thun und Frankfurt am Main, 2001).
- [93] A. Huang *et al.*: *Micro. Mesopor. Mater.* **130**, 352–356 (2010).
- [94] R. Krishna & J. M. van Baten: *Micropor. Mesopor. Mat.* **137**, 83–91 (2011).

- [95] D. M. Ruthven & S. C. Reyes: *Micropor. Mesopor. Mat.* **104**, 5966 (2007).
- [96] A. Huang & J. Caro: *Micropor. Mesopor. Mat.* **129**, 90–99 (2010).
- [97] N. Hedin *et al.*: *Micropor. Mesopor. Mat.* **109**, 327–334 (2008).
- [98] N. Hedin *et al.*: *Micropor. Mesopor. Mat.* **98**, 182–188 (2007).
- [99] F. Hibbe *et al.*: *J. Am. Chem. Soc.* **134**, 7725–7732 (2012).
- [100] S. Brandani *et al.*: *Zeolites* **15**, 494–495 (1995).
- [101] A. Corma *et al.*: *Nature* **431**, 287 (2004).
- [102] W. Heink *et al.*: *J.C.S. Faraday Trans.* **88**, 3505–3509 (1992).
- [103] D. M. Ruthven: *Chem. Ing. Tech.* **83**, 4452 (2011).

Chapter 7

Attachment

7.1 Curriculum Vitae

Persönliche Daten

- Name: Florian Christoph Hibbe
- Geboren am 01. Januar 1983 in Soltau (Niedersachsen)
- verheiratet mit Corinna Hibbe, geb. Schwel
- Email: hibbe@physik.uni-leipzig.de

Schulbildung

- 1989 – 1995 Besuch der Grundschule und Orientierungsstufe in Soltau
- 1995 – 2002 Besuch des Gymnasiums in Soltau
- 2002 Abitur (Note 2,3)

Studium

- 2003 – 2008 Studium Diplom-Physik an der Universität Leipzig
- 2007/2008 Diplomarbeit zum Thema "Interferenzmikroskopische Untersuchung der Temperaturabhängigkeit transientser Konzentrationsprofile in nanoporösen Materialien"
- 10/2008 Abschluss Dipl.-Phys. (Note 1,1)
- seit 11/2008 Promotion; Universität Leipzig, Abteilung Grenzflächenphysik;
Betreuer: Prof. Dr. Jörg Kärger
Arbeitsthema: "FTIR Microscopy as a Tool for Studying Molecular Transport in Zeolites"

Sonstiges

- 2002/2003 Zivildienst an der Sozialstation Fallingbösel
- 11/2011 Forschungsaufenthalt an der School of Chemistry, University of Manchester

7.2 Danksagung

Folgenden Menschen gilt mein aufrichtiger Dank in Bezug auf die Fertigstellung dieser Arbeit und die angenehme, an der Universität Leipzig verbrachte, Zeit meiner Promotion:

Dem Betreuer meiner Promotion, Prof. Jörg Kärger, von dem ich in den letzten Jahren vieles nicht nur in fachlichen sondern auch in zwischenmenschlichen Dingen lernen konnte.

Den unermüdlichen Produzenten der Materialien, deren Untersuchung ihrer Transporteigenschaften der Großteil dieser Arbeit gewidmet ist und die mich immer wieder mit neuen oder modifizierten Vertretern ihrer Kreationen versorgt haben: Prof. Jürgen Caro (Leibniz Universität Hannover), Prof. Jens Weitkamp (Universität Stuttgart) und Prof. Jing Li (Rutgers University, Piscataway USA) sowie ihren Mitarbeitern und Studenten.

Prof. Michael Anderson (Manchester University) für den angenehmen Aufenthalt und die erfolgreiche Arbeit in seiner Arbeitsgruppe in Manchester.

Der Abteilung Grenzflächenphysik der Universität Leipzig, insbesondere den Angehörigen der allmontaglichen Mikroskopierunde Dr. Christian Chmelik, Tomas Binder und Tobias Titze für Diskussion, Kaffee und Kekse sowie Stefan Schlayer, ebenfalls für angenehme Unterhaltung und technischen Support.

Der International Research Training Group (IRTG) "Diffusion in Porous Materials" für fachliche und finanzielle Unterstützung.